Characterization of the Amazon Rainforest Backscatter at X-Band Using TanDEM-X Data

Luca Dell'Amore, José–Luis Bueso–Bello, Patrick Klenk, Jens Reimann, and Paola Rizzoli

***Abstract*—The radiometric calibration of spaceborne SAR products plays a key role for ensuring a good performance of the whole end-to-end system and requires a precise knowledge of both the radar system and the illuminated target on ground. The shape of the antenna pattern in elevation can be directly estimated by analyzing SAR detected images in presence of a homogeneous and flat backscatter profile in the slant range dimension. To this aim, tropical rainforests have been established by the SAR community as well-known calibration sites for performing such an activity. Here, according to the hypothesis of isotropic scattering, the backscattering coefficient in terms of unit area perpendicular to the antenna, called gamma nought, is assumed to remain constant with respect to the incidence angle. Nevertheless, several studies using X- and C-band sensors have shown a slight dependency of the backscatter on the incidence angle, as well as on ground target properties and meteorological conditions. In this work, we present a detailed statistical characterization of radar backscatter at X-band over the Amazon rainforest using TanDEM-X data and we provide insights on how to best utilize radar backscatter data in this region for SAR calibration and modeling purposes. In particular, we concentrate on the dependency of the Amazon rainforest backscatter on the day-time of acquisition, which is directly related to the orbit direction of TanDEM-X. Furthermore, we analyze the seasonal variation of the radar backscatter, as well as possible radiation variations over different locations in the Amazon, characterized by different climate conditions and biomes. Finally, we provide a series of backscatter models for different scenarios, which can be used, e.g., for X-band spaceborne SAR system design and theoretical modeling.**

***Index Terms*—Amazon rainforest, SAR calibration, synthetic aperture radar (SAR), TanDEM-X (TDX).**

I. Introduction

SYNTHETIC aperture radar (SAR) systems represent nowadays a well-recognized technique in the field of remote sensing, thanks to their capability to operate in presence of clouds and independently of day-light and weather conditions. They are able to acquire high-resolution images of the Earth's surface and to provide useful data for a large variety of scientific applications, ranging from the assessment of physical phenomena to the monitoring of Earth's surface dynamics.

One of the key components for ensuring a high quality of the derived SAR images is an accurate absolute calibration of the system [1], [2], [3], [4], [5], [6], [7], [8]. The absolute calibration of a SAR sensor allows for translating the focused signal amplitude, called digital number, to a physical quantity, such as the scattering coefficient. Typically, it is performed after launch using on-ground reference targets, such as transponders and corner reflectors, which provide a precisely known reference radar cross section. Differently, the elevation antenna pattern is characterized during the prelaunch phase by using on-ground measurements of the instrument itself. However, because of increasing SAR systems complexity, the antenna pattern shape needs to be accurately estimated and monitored through in-flight campaigns as well. This is accomplished by acquiring SAR data over homogeneous distributed targets, under the assumption of isotropic scattering. The shape of the antenna pattern is then clearly visible in the focused detected images. In particular, tropical rainforests, such as the Amazon and Congo forests, have been established by the SAR community as well-known test sites for SAR calibration [9], [10], [11], [12], [13], [14], [15], [16], [17], [18], [19], [20], thanks to their homogeneous and almost-isotropic signature. Nevertheless, several studies conducted in C-band, e.g., using the ASCAT C-band scatterometer [21] and the RADARSAT-2 C-band SAR sensor [22], and in X-band with the TanDEM-X mission (TDM) [23], have shown a slight dependency of the backscatter on the incidence angle, as well as on ground target properties, and meteorological conditions [5], [24], [25].

TerraSAR-X (TSX) and TanDEM-X (TDX) are two twin satellites developed and operated in a public/private partnership between the German Aerospace Center (DLR) and Airbus Defence and Space. The TerraSAR-X mission started in June 2007 and combines the ability of acquiring monostatic SAR images with different acquisition modes, ranging from high-resolution spotlight to wide-swath scanSAR imaging [26], [27], [28]. The TDM started in 2010 with the launch of the TDX satellite, which joined TSX in a close orbit formation, and it is currently the only spaceborne bistatic SAR mission at X-band [29], [30], [31], [32]. It enables the generation of highly accurate across- and along-track single-pass interferometric products at X-band with variable baselines, polarizations, and acquisition modes. Beside the primary target of the mission, i.e., the generation of a worldwide high-precision digital elevation model (DEM) [33], [34], [35], [36], a variety of scientific works have benefited from the availability of TDX bistatic data, ranging from biosphere- and hydrosphere- to geosphere- and cryosphere-related applications (e.g., [37], [38], [39], [40], [41], [42], [43], [44], [45], [46], [47], [48], [49], [50], [51], [52], [53], [54], [55]).

In this article we present a detailed statistical characterization of X-band radar backscatter over the Amazon rainforest using TDX data at large scale. The rest of this article is organized

Manuscript received 29 June 2023; revised 15 September 2023 and 9 November 2023; accepted 20 November 2023. Date of publication 4 December 2023; date of current version 20 December 2023. *(Corresponding author: Luca Dell'Amore.)*

The authors are with the Microwaves and Radar Institute, German Aerospace Center, 82234 Wessling, Germany (e-mail: luca.dellamore@dlr.de; Jose-Luis.Bueso-Bello@dlr.de; patrick.klenk@dlr.de; jens.reimann@dlr.de; paola.rizzoli@dlr.de).

Digital Object Identifier 10.1109/JSTARS.2023.3338982

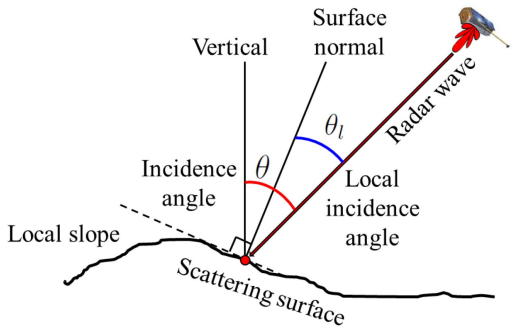

Fig. 1. Reference geometry for the incidence angle θ and for the local incidence angle θ_l.

as follows. Section II and III present the utilized backscatter mapping quantities and the considered data sets, respectively. In Section IV, we concentrate on the equatorial Amazon rainforest; specific considerations are drawn regarding the backscatter dependency on the day-time of acquisition and orbit direction, whereby descending and ascending orbit acquisitions are generally acquired in the morning and in the evening, respectively. Section V investigates the seasonal variations of the radar backscatter over the equatorial Amazon rainforest by comparing data acquired during dry and wet seasons. In Section VI we analyze different locations in order to characterize the Amazon rainforest depending on latitude positions and, therefore, on different climate conditions and biomes at large scale. Moreover, a temporal stability analysis on the rainforest radiation is also provided by considering data sets collected over the same area but spread over a time span of several years. In Section VII, we characterize the radar backscatter over few test sites in the Amazon rainforest for other polarization channels as well. In Section VIII we provide a series of backscatter models for different scenarios. Some considerations about the well-known and widely used Ulaby and Dobson models in [56] are also drawn. A discussion on the results follows in Section IX. Finally, Section X concludes this article. A summary of all evaluated backscatter statistical parameters is reported in the Appendix.

II. Backscatter Mapping Quantities

Typically, the quantity used for measuring and analyzing backscatter levels in SAR data over rainforests is the backscattering coefficient gamma nought $\gamma^0(\theta_l)$, which can be expressed as

$$\gamma^0(\theta_l) = \beta^0(\theta)\tan\theta_l \tag{1}$$

where $\beta^0(\theta)$ is the radar brightness, θ the slant range-dependent incidence angle, which monotonically increases from near to far range, and θ_l the local incidence angle, which depends on the observed topography, as depicted in Fig. 1. In particular, $\gamma^0(\theta_l)$ describes the reflectivity of distributed targets per unit area of the incident wave front. Unlike the more popular scattering projection $\sigma^0(\theta_l)$, i.e., radar reflectivity per unit area on ground, γ^0 decreases the sensitivity of the cross section to the incidence angle and it has the property of maintaining a relatively flat backscatter profile over a wide range of incidence angles for very dense and homogeneous volumetric targets [57], [58]. This is the case of the Amazonas, where the γ^0 profile over the local incidence angle can be considered as an isotropic scattering measure. The radar brightness $\beta^0(\theta)$ in (1), i.e., radar reflectivity per unit pixel area, is directly derived through the absolute calibration of the focused SAR data as

$$\beta^0(\theta) = \frac{(\mathrm{DN}(\theta))^2}{K} \tag{2}$$

with DN being the recorded digital number and K the absolute calibration constant. Its computation does not require the knowledge of local incidence angle.

In order to avoid confusion, in the following sections the backscatter characterization will rely on the local incidence angle θ_l as independent variable. Therefore, a precise knowledge of the underlying topography is required in order to precisely estimate the local incidence angle as $\theta_l = \theta - \alpha$, with α being the local terrain slope in the slant range direction.

III. Amazon Rainforest Data Set

The vast majority of TDX acquisitions was acquired using horizontal polarization in transmit as well as in receive, i.e., (HH) polarization. Overall, we processed 3723 SAR images acquired over the Amazon rainforest in stripmap mode in HH polarization, at almost-full resolution, i.e., 6 m $\times$6 m, using the experimental TDX interferometric processor [59]. Unlike previous works concerning TDX backscatter analysis [23], [34], which relied on quicklook images at 50 m resolution in order to limit the computational burden when considering large data sets [60], the use of almost-full resolution data allows for a reliable estimation of the complete signal dynamics as explained in [23]. First, we absolutely calibrated each image in order to retrieve β^0. As exhaustively described in [1], [2], [3], [4], [5], and [6], the TSX and TDX systems were absolutely calibrated with an outstanding accuracy of 0.39 dB and 0.48 dB, respectively; in-orbit calibration and dedicated activities were performed during the commissioning phase by exploiting reference point targets on ground (transponders and corner reflectors). Then, we generated the corresponding local incidence angle map θ_l using the annotated satellite orbit position and the TDX global edited DEM [61], which is currently the most accurate DEM available at global scale. Note that the use of a precise external DEM allows for properly dealing with local terrain depressions/valleys and, more in general, with local higher relief terrain. Some considerations can be formulated regarding the reliability of the reference DEM: Given the interpolation from the original 30 m to the current 6 m resolution, it is reasonable to assume that DEM measurements are somehow smoothed, thus, mitigating possible local height errors. Also, the TDX global DEM provides an estimation of the topographic height corresponding to the location of the mean phase center within a resolution cell and is the result of the mosaicking of multiple acquisitions. This procedure also mitigates the impact of possible outliers. Moreover, it is worth noting that both the current analysis and the reference DEM are based on data from the same sensor, i.e., TDX, so that we can assume the consistency of the measurements between the considered backscatter data and the underlying DEM product. In particular, given the same radar central frequency and system parameters and assuming the Amazon rainforest to be composed of dense vegetation, we rely on the assumption that the measured radiation in both cases mostly comes from the upper layers of the canopy [62], [63]. Finally, possible residual errors in the estimation of the local terrain slope α and, consequently, of the local incidence angle θ_l, are not expected to significantly bias

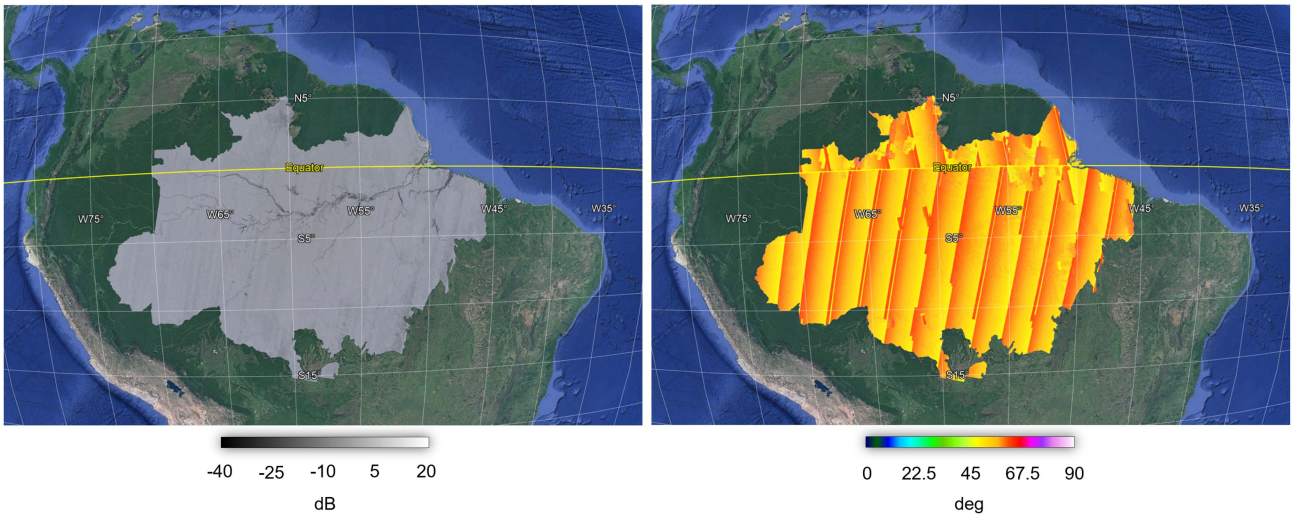

Fig. 2. γ^0 (left) and θ_l (right) mosaics over the whole Amazon rainforest visualized on GoogleEarth. They are composed using TDX stripmap data in HH polarization and acquired in 2012/2013 with steep/shallow incidence angles.

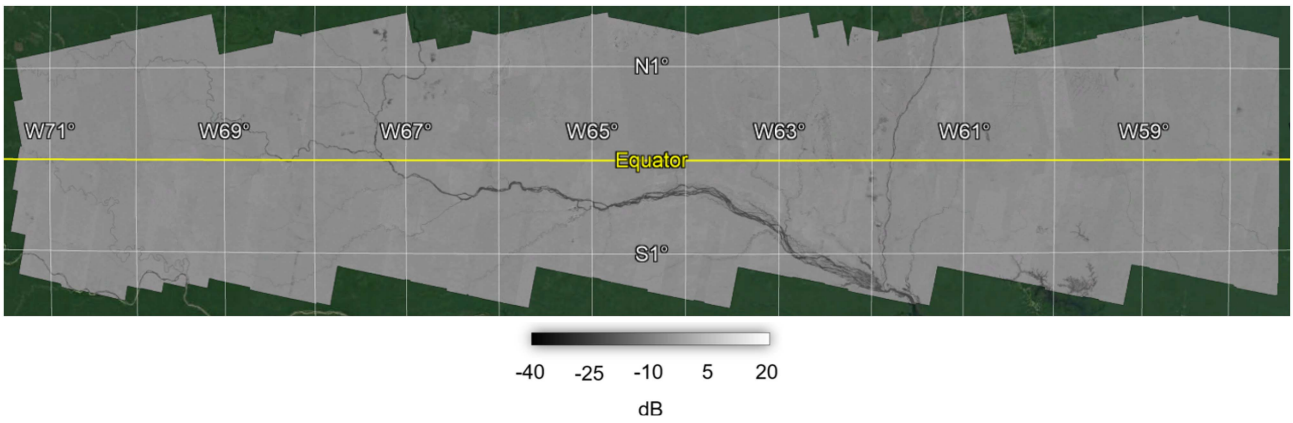

Fig. 3. γ^0 mosaic over the equatorial Amazon rainforest, corresponding to test site (a) in Table I, visualized on GoogleEarth. It is composed by the complete TDX data set of stripmap, HH polarization data acquired between December 2010 and September 2014.

the final results, given the predominant low-relief topography characterizing the Amazon rainforest. As a final step, we computed γ^0 by applying (1). Both γ^0 and θ_l are, then, geocoded and interpolated on a common latitude/longitude grid in order to generate large-scale mosaics.

Fig. 2 shows γ^0 (left) and θ_l (right) mosaics over the whole Amazon rainforest, which were composed using TDX images acquired between 2012 and 2013 with shallow/large incidence angles. Given the low-relief topography of the Amazon rainforest basin, it can be seen that the local incidence angle map reasonably approximates the slant-range dependent incidence angle. Moreover, the two orbit direction geometries are clearly visible, where data in the Northern Hemisphere were mostly acquired in ascending orbit direction, whereas data in the Southern Hemisphere in descending one [29], [64]. Moreover, given the sun-synchronous, dawn-to-dusk orbit of the TDM, descending and ascending orbit acquisitions are typically acquired in the morning and in the evening, respectively.

The analyses in the following sections are spread over different locations of the Amazon rainforest. As first investigation, we considered the equatorial rainforest between $[-71°, -58°]$ longitude and $[-1.5°, 1.5°]$ latitude, which comprises images acquired using all twenty nominal TDX beams, i.e., all TDX ascending/descending geometries, used for the generation of the global DEM [35], [36]. Here, we utilized the complete data set acquired from December 2010 to September 2014 (consisting of 1998 acquisitions) for characterizing the backscatter dependency with respect to orbit direction and seasonality. The area is depicted in Fig. 3. Afterward, we considered different regions of the Amazon rainforest, characterized by different climate conditions and biomes [65], [66], [67], [68], [69], [70]. We concentrated on three different test sites, which differ in latitude, comprised between $[0°, 2°]$, $[-4°, -2°]$, and $[-8°, -6°]$, respectively, whereas sharing the same longitude span between $[-71°, -58°]$. The location of the considered areas is presented in Fig. 4. Note that each data set is within a 2° latitude span and does not overlap with the others, which is a reasonable setting in order to properly separate the different test sites depending on local conditions at large scale. In particular, this is a compromise between the number of available data and the large-scale diversity between the observed

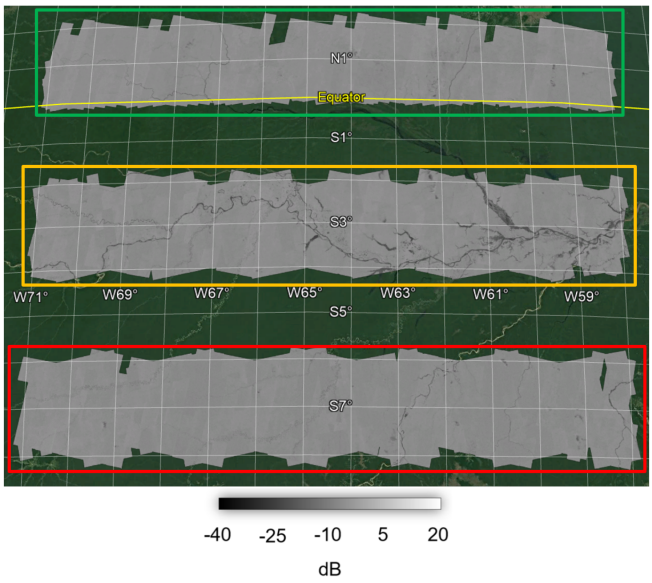

Fig. 4. γ^0 mosaic over test sites (b) and (c), and (d) in Table I, visualized on GoogleEarth. It is composed by the corresponding complete TDX data sets of stripmap, HH polarization data reported in the table. The three test sites are identified by colored boxes, i.e., (b) green, (c) orange, and (d) red.

TABLE I
DATA SETS USED FOR THE CURRENT INVESTIGATIONS USING IMAGES IN HH POLARIZATION

	Longitude	Latitude	Time information
(a)	$[-71°, -58°]$	$[-1.5°, 1.5°]$	Dec. 2010 – Sept. 2014
(b)	$[-71°, -58°]$	$[0°, 2°]$	Dec. 2010 – Sept. 2014, 2018–2019
(c)	$[-71°, -58°]$	$[-4°, -2°]$	2011–2012, 2018–2019
(d)	$[-71°, -58°]$	$[-8°, -6°]$	2011–2012, 2018–2019

Note: each test site is identified by longitude/latitude coordinates. Acquisition time interval is reported as well.

areas, due to potential differences in climate conditions and biomes. Moreover, we assume that the transition between different locations in the Amazon rainforest is smooth, so that γ^0 backscatter estimations over missing latitudes could be reasonably interpolated. Of course, local phenomena could occur and play a role, but are anyway expected to be averaged given the large-scale nature of the investigation. The last two data sets, acquired in the Southern Hemisphere, consist of data acquired in descending and ascending orbit directions in 2011–2012 and 2018–2019, respectively. Here, ascending orbit acquisitions were made possible, thanks to a swap of the TSX and TDX satellites, which took place in September 2017 [64]. However, given the sun-synchronous and dawn-to-dusk orbit of TDX, descending/ascending orbit acquisitions were still performed during morning/evening, respectively. Therefore, we always combined data depending on the day-time of acquisition. As far as the test site between $[0°, 2°]$ latitude is concerned, ascending orbit acquisitions were retrieved from the investigated data set depicted in Fig. 3, whereas descending orbit data were acquired after the satellites swap, in 2018–2019. Table I summarizes all data sets used for the current investigations. In particular, the table reports the latitude/longitude locations of each test site, together with the acquisition time interval. By considering the three latitude intervals, a temporal stability analysis on the γ^0 backscatter was performed in order to ensure the comparability between the results from ascending/descending orbit acquisitions, as data acquisition times are very different. To this aim, the long-term temporal radiation stability was analyzed over a small test site used for long-term system monitoring (LTSM) tasks during the TDM. The area is depicted within the white box in Fig. 5. In particular, a time-series of 178 data takes was collected between 2011 and 2019, with all data acquired in the morning (in descending orbit configuration) and in HH polarization.

Since all nominal TDX acquisitions are acquired in HH polarization, the core of the present analysis concentrates on data acquired in this polarization. Further considerations on other polarization channels are presented in Section VII. Very few images were collected using the other channels, i.e., vertical polarization in transmit as well as in receive (VV) and horizontal polarization in transmit and vertical in receive (HV), resulting in limited data sets. These are depicted in Fig. 5, where data takes were repeatedly performed for LTSM purposes over selected test sites, identified by the cyan (VV) and green (HV) boxes. Overall, 156 single polarization stripmap SAR images, among which 146 in VV and 10 in HV polarization, were collected between November 2010 and September 2014. Note that the orange box identifies test site (c) in Table I, which is used as reference HH data set for comparison purposes between different polarization channels.

IV. γ^0 Dependency on the Local Incidence Angle

In this section, we concentrate on the equatorial Amazon rainforest corresponding to test site (a) in Table I, and we present a large-scale analysis for the characterization of γ^0 at X-band with respect to the local incidence angle θ_l. The corresponding γ^0 mosaic is depicted in Fig. 3. The whole range of nominal local incidence angles θ_l, which extends from about 25° to about 51°, was sampled with angular intervals of 1°. γ^0 samples, which belong to each single interval were then grouped together, allowing for the derivation of distribution statistics, such as mean and median γ^0, its standard deviation (SD) and percentiles. Moreover, we applied the TDX Forest/NonForest (FNF) map [50] in order to select forested pixels only. Given the very different resolution of the FNF map ($50\,\mathrm{m} \times 50\,\mathrm{m}$) compared with the considered γ^0 backscatter data, we eroded forested areas with a square kernel of 5×5 pixels in order to avoid misclassification at the borders. For each incidence angle interval, possible outliers were removed by taking only the backscatter distribution between the 1st and 99th percentiles.

The obtained results are presented in Fig. 6 for both data acquired in the morning, i.e., descending orbit acquisitions, and in the evening, i.e., ascending orbit ones.[1] In particular, the figure shows the γ^0 backscatter distributions with respect to each interval of local incidence angles. The boxes extend from the lower to upper quartile values of the data distribution, i.e., from the 25th to 75th percentiles, with whiskers reaching the 5th and 95th percentiles. The solid line within each box

[1]TDX data takes were operationally acquired in ascending orbit direction in the Northern Hemisphere, whereas in descending in the Southern one. Because of a satellites swap in September 2017 [64], the acquisition planning changed, with ascending and descending data takes acquired in the Southern and Northern Hemispheres, respectively.

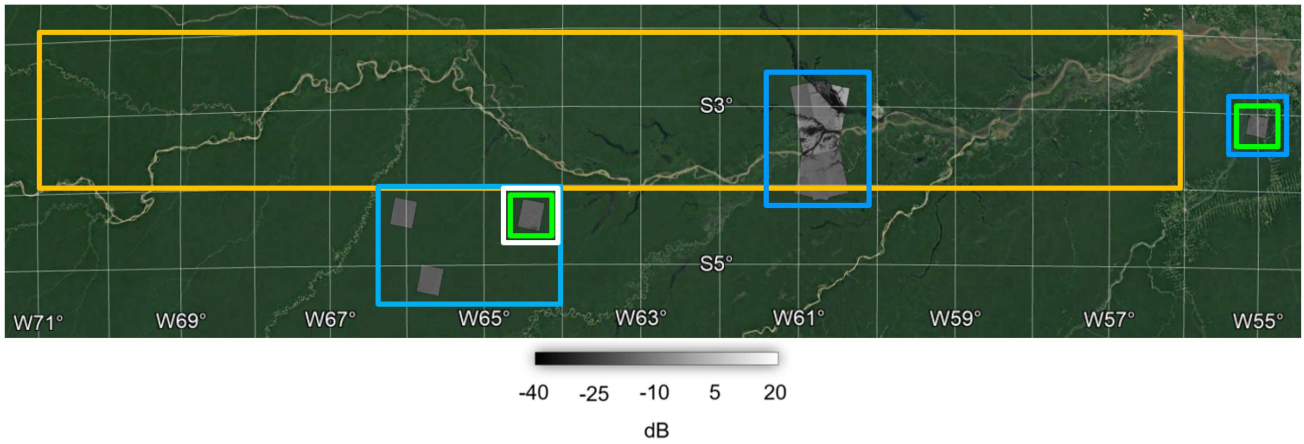

Fig. 5. γ^0 mosaic over LTSM test sites in the Amazon rainforest, visualized on GoogleEarth. It is composed by TDX data takes acquired in stripmap mode in VV (cyan boxes) and HV (green boxes) single polarizations, between November 2010 and September 2014. Orange box identifies test site (c) in Table I. Moreover, the white box identifies the LTSM region used for the long-term temporal stability analysis on the γ^0 radiation.

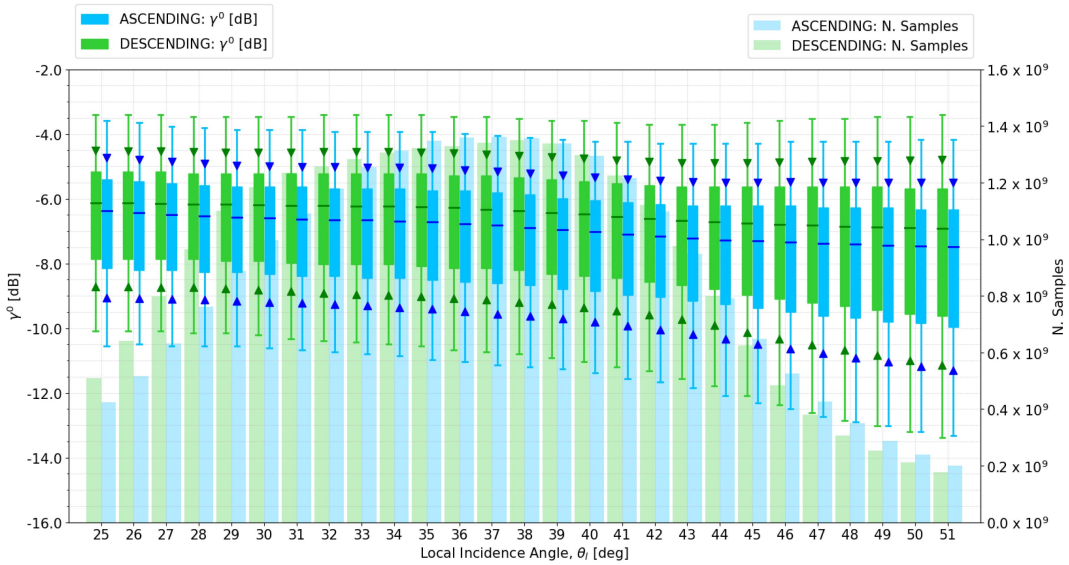

Fig. 6. γ^0 backscatter distributions with respect to each interval of local incidence angles. Data distributions are shown for both data acquired in the morning, i.e., descending orbit acquisitions, and in the evening, i.e., ascending orbit ones. Each box extends from the lower to upper quartile values of the data distribution, i.e., from the 25th to 75th percentiles, with whiskers reaching the 5th and 95th percentiles. The solid line within each box indicates the mean value of the distribution, with triangles identifying the SD confidence interval of each data group, i.e., from mean $-$SD to mean $+$SD. The histograms depicting the number of samples used for the derivation of the backscatter statistical parameters are reported as well in the background.

indicates the distribution mean value, with triangles identifying the SD confidence interval of each data group, i.e., from mean $-$SD to mean $+$SD. Note that all the statistics were computed in linear scale and only afterward were converted to dB. The corresponding histograms depicting the number of samples used for the derivation of the backscatter statistical parameters are shown in the background. The figure demonstrates the nonperfectly-isotropic nature of the Amazon rainforest, as the backscatter profiles are not completely flat over the full range of incidence angles. Moreover, ascending and descending orbit acquisitions show a different behavior: Acquisitions performed in the morning present higher backscatter values, with a bias of about 0.5 dB, when compared with the ones acquired in the evening. Also, it can be seen that the backscatter variability increases when considering larger incidence angles.

Finally, all statistical parameters derived in this analysis as well as in the following sections are provided in the Appendix.

V. γ^0 Seasonal Variability

This section investigates the seasonal variability of the radar backscatter over the equatorial Amazon rainforest presented in Fig. 3, by comparing dry and wet seasons. The statistical analysis relies on the same procedure described in Section IV and was performed for ascending and descending orbit acquisitions separately. For this investigation, the dataset (a) in Table I was first split between ascending and descending orbit data. Second, the two derived data sets were subsampled by considering data acquired during dry and wet seasons only. For this scope, we assumed as dry the months between June and September, whereas

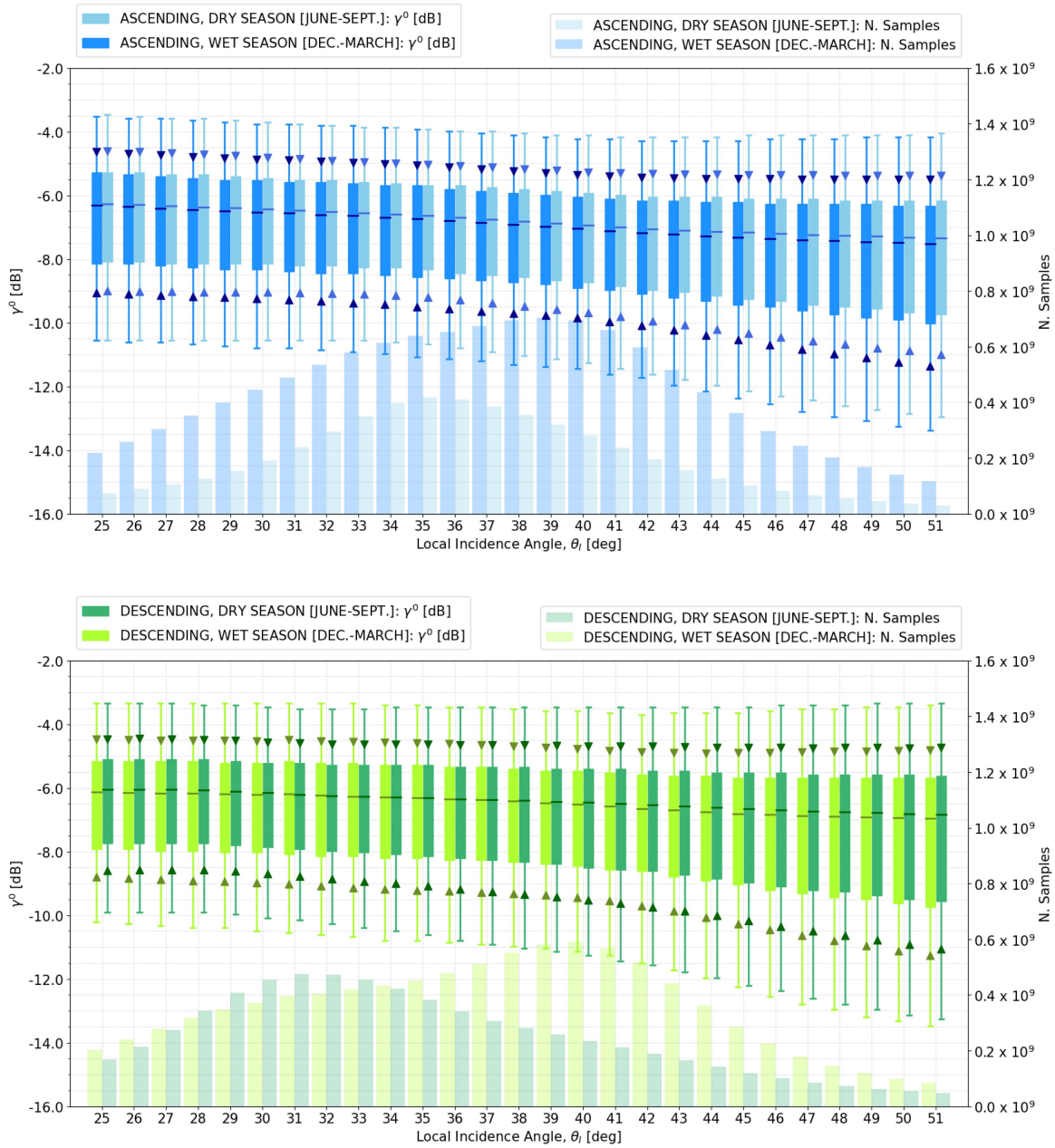

Fig. 7. Seasonal variability of the γ^0 radar backscatter with respect to local incidence angles, by comparing dry and wet seasons. Dry season is defined as the period between June and September, whereas the wet season is comprised between December and March. Data distributions are shown for both evening/ascending orbit (top) and morning/descending orbit (bottom) acquisitions. Each box extends from the 25th to 75th percentiles of the data distribution. For each interval, the solid line represents the γ^0 mean value, with triangles identifying the SD confidence interval between mean $-$SD and mean $+$SD; whiskers indicate the 5th and 95th percentiles. The histograms depicting the number of samples used for the derivation of the backscatter statistical parameters are reported as well in the background.

wet acquisitions were collected starting from December until March [71], [72], [73], [74].

Fig. 7 shows the resulting γ^0 distributions with respect to local incidence angles. Unlike the previous investigation in Section IV, where distributions of γ^0 were derived from a quite balanced number of samples between ascending and descending orbit acquisitions, the radar backscatter from dry and wet seasons is characterized by unbalanced data sets. Nevertheless, this aspect is not expected to bias the estimation, given the large amount of available data for each case, even for the worst-case local incidence angles interval, consisting of around 30 million samples. This could be verified by looking at the standard error of the mean (SEM) in the corresponding table in the Appendix (Table III). Clearly, a more precise estimation of the sample mean is achieved in presence of larger data sets. Nevertheless, as suggested by the SEM values in the tables, the estimated mean values are derived with great precision in all cases, so that small differences between different data groups are not expected to significantly impact the final results. The analysis shows that no significant difference between the two seasons is

detectable. Whereas, it is worth noting that the main driver of the γ^0 radar backscatter variation over the Amazon rainforest remains the day-time of acquisition, as an overall offset of about 0.5 dB can still be seen between descending (morning) and ascending (evening) orbit data. As already mentioned in the previous section, a larger backscatter variability can be observed as moving toward larger incidence angles.

VI. γ^0 Analysis of Different Amazon Locations

In the following, we focus on three different locations in the Amazon rainforest, characterized by different latitude positions and, therefore, by different climate conditions and biomes at large scale [65], [66], [67], [68], [69], [70]. In order to do so, we consider the three test sites, i.e., (b), (c), and (d) in Table I, which correspond to the green, orange, and red boxes in Fig. 4, respectively. As previously done in Section V, the investigation was performed for ascending and descending orbit acquisitions separately.

The obtained results are presented in Fig. 8 for both data acquired in the evening/ascending orbit (top) and in the morning/descending orbit (bottom). The γ^0 backscatter distributions are shown with respect to each interval of local incidence angles and for the three different test sites, confirming the nonperfectly-isotropic nature of the Amazon rainforest. Even though a different amount of data is available for each test site, statistics were derived from a large amount of samples, as proven by the order of magnitude of the corresponding histograms and, therefore, are not expected to be significantly biased. Different behaviors can be observed for the different test sites by comparing ascending and descending orbit images. The γ^0 backscatter distributions look similar to each other, when considering data acquired in the evening, i.e., acquired in ascending orbit direction; a small bias can be detected in case of smaller incidence angles, with test site (d) showing slightly lower backscatter values on average, whereas the three backscatter distributions converge as moving toward far-range geometries. On the other hand, test sites (c) and (d) appear less stable compared with (b) [near- and far-range log-backscatter difference around 0.65 dB (b), 1.59 dB (c), and 1.15 dB (d)] when considering data takes acquired in the morning, i.e., with a descending orbit configuration. Here, despite remaining quite stable up to middle-range incidence angles, the backscatter mean value significantly drops as moving toward larger angles. There, the backscatter variability increases and the two distributions converge to similar values. Moreover, a higher backscatter variability can be detected on average during night/morning, i.e., from descending orbit acquisitions. In order to ensure the comparability between ascending/descending orbit results, as they correspond to very different data acquisition times, a long-term temporal radiation stability analysis was also performed over the small test site depicted in the white box in Fig. 5. In particular, data were grouped together depending on seasonality and, consequently, considering similar local conditions. Moreover, as exhaustively discussed in [16], [17], [18], and[19], no significant trends or radiometric degradation have been observed in TSX and TDX systems since launch. LTSM measurements and extended analyses have shown a stable performance of all parameters, confirming the outstanding radiometric stability of the instrument. As a consequence, eventual and significant γ^0 radiation variations are assumed to be related to the nonstationary behavior of the Amazon rainforest itself. The obtained results are presented in Fig. 9. Note that no data were acquired between 2015 and 2016. The plot confirms a substantial backscatter stability over time for both seasons, with a log-backscatter deviation of 0.2 dB and 0.11 dB for dry and wet periods, respectively. Furthermore, as already discussed in Section V, no significant difference between the two seasons behavior is detectable, with dry and wet periods showing an almost-equal backscatter average over time of –6.81 dB and –6.83 dB, respectively. An analysis on the dependency of the γ^0 backscatter on the seasonal acquisition period, not shown here for the sake of brevity, was performed as well for the three considered locations. As outcome, similar conclusions as in Section V can be formulated, where no significant difference between the two seasons behavior is detectable. Nevertheless, special attention has to be paid on test sites (c) and (d), in case of morning/descending orbit data takes. As discussed above for the general case depicted in Fig. 8, the two test sites seem to be less stable during night/morning with respect to local incidence angles. Similar instabilities can then be observed as well in the corresponding backscatter angular profiles, depending on the considered season.

VII. γ^0 Behavior for Other Polarizations

A comparison of the radar backscatter between HH, VV, and HV polarizations, with respect to the local incidence angle and the orbit direction, is shown in Fig. 10. The corresponding histograms, depicting the number of samples used for deriving the backscatter statistical parameters, are depicted in Fig. 11. It is worth noting that VV and HV samples are not uniformly distributed over the full range of incidence angles, given the limited number of available acquisitions. The analysis shows an almost constant offset of about 0.5 dB between HH and VV channels over data takes acquired with an ascending orbit geometry, i.e., evening acquisitions, with the VV polarization showing lower backscatter values. On the other hand, this offset gets smaller for descending orbit data takes, i.e., morning acquisitions, as moving toward middle- and far-range geometries. In this case, an almost negligible difference between HH and VV polarizations is observed. Given the considerable polarimetric calibration accuracy between the two copolarized channels, performed using reference targets [4], no polarimetric amplitude imbalance is expected to affect the final results by introducing a systematic bias. Therefore, possible differences between polarizations are expected to be simply related to different scattering mechanisms within the canopy and/or to external local conditions. Regarding the HV cross-polarization channel, the radar backscatter significantly drops compared with the HH and VV copolarizations, with differences up to 7 dB for all the investigated scenarios. It is worth noting that acquisitions performed in the evening and in HV polarization show a very stable radar backscatter, with negligible variations over the entire range of illuminated incidence angles.

VIII. γ^0 Empirical Modeling

In this section, we derive a series of empirical X-band backscatter models over the Amazon rainforest, based on the analyzed TDX data. In particular, we concentrate on the test sites described in Table I, focusing on the γ^0 dependency on

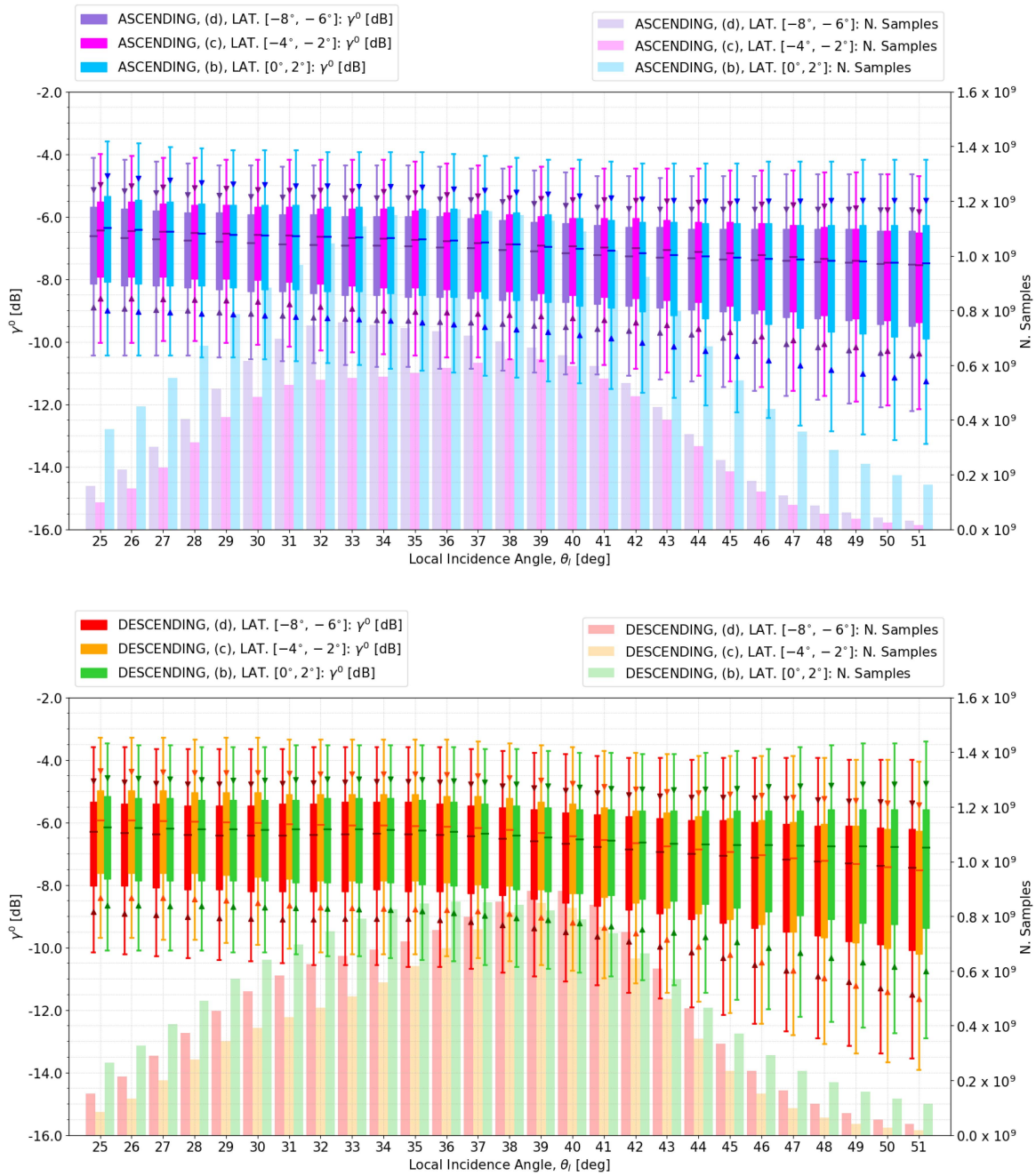

Fig. 8. γ^0 backscatter characterization of different Amazon locations with respect to local incidence angles. Data distributions are shown for both evening/ascending orbit (top) and morning/descending orbit (bottom) acquisitions. Each box identifies the confidence interval between the 25th and 75th percentiles of the backscatter distribution, with the solid line being the mean value of the total set of samples. Triangles indicate the SD confidence interval between mean −SD and mean +SD, whereas whiskers correspond to the 5th and 95th percentiles. Histograms depicting the number of samples used for the derivation of the backscatter statistical parameters are presented as well in the background.

the day-time of acquisition and on seasonal variability, as reported in Sections IV, V, and VI. Backscatter models for VV and HV polarizations are derived as well. For this scope, the angular dependency of the γ^0 mean value (dB), i.e., $\hat{\gamma}^0_{\text{mean}}(\text{dB})$, is determined by an iterative least-squares, nonlinear curve-fitting approach. Given the wide utilization in the literature of the models provided by Ulaby and Dobson in [56] and since the radar radiation principles on which they were built still stand, we decided to rely on the same curve-fitting formulation. Accordingly, the nonlinear fitting function consists of the sum of an exponential and a cosine term, which allows for a precise representation of the nonlinear fluctuations of the radar backscatter, while maintaining its overall decreasing behavior over incidence angles. The underlying model formulation is given by

$$f(\theta_1) = P_1 + P_2 e^{-P_3\theta_1} + P_4 \cos(P_5\theta_1 + P_6) \tag{3}$$

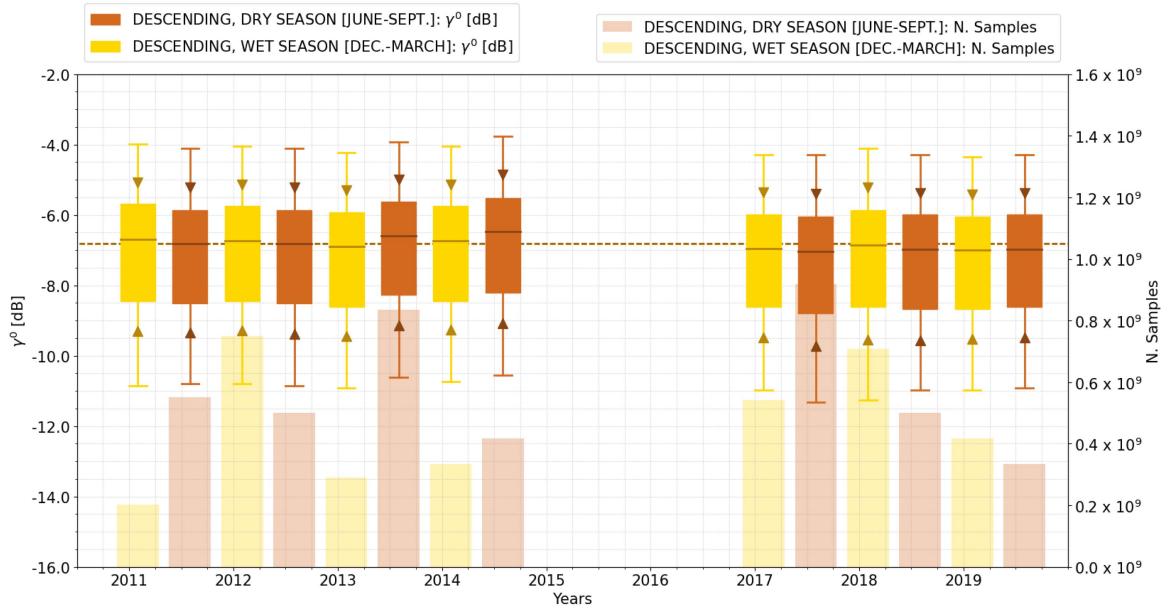

Fig. 9. Long-term temporal stability analysis of γ^0 radiation. Data distributions are shown for morning/descending orbit acquisitions only. Each box extends from the 25th to the 75th percentiles of data distribution, with whiskers reaching the 5th and 95th percentiles. Solid line within each box indicates the estimated mean value of the population, with triangles showing the SD confidence interval between mean $-$SD and mean $+$SD. Two almost-fully-overlapping dashed horizontal lines report the estimated mean values average over time, computed in linear scale, and then converted to dB. Histograms depicting the corresponding number of samples are reported as well in the background.

TABLE II
RESULTING FITTING PARAMETERS CORRESPONDING TO THE γ^0 DISTRIBUTIONS IN FIGS. 6, 7, 8, AND 10

Orbit Direction	Polarization	Season	Coordinates		Angular Range		γ^0 Fitting Parameters					
			Longitude	Latitude	$\theta_{l,\min}$	$\theta_{l,\max}$	P_1	P_2	P_3	P_4	P_5	P_6
Ascending	HH	\	$[-71°, -58°]$	$[-1.5°, 1.5°]$	25°	51°	0.2636	−5.6081	−0.3740	0.0625	22.4724	−14.0307
Ascending	HH	Dry	$[-71°, -58°]$	$[-1.5°, 1.5°]$	25°	51°	3745.9951	−3751.1270	−0.0007	0.0515	17.5496	−10.0293
Ascending	HH	Wet	$[-71°, -58°]$	$[-1.5°, 1.5°]$	25°	51°	4478.7019	−4483.7144	−0.0006	0.0448	20.7643	−12.4700
Ascending	HH	\	$[-71°, -58°]$	$[0°, 2°]$	25°	51°	7.9468	−13.1752	−0.1817	0.0635	22.6588	−14.2112
Ascending	HH	\	$[-71°, -58°]$	$[-4°, -2°]$	25°	51°	−5.8394	−0.2207	−2.2891	−0.0142	20.7231	−13.2585
Ascending	HH	\	$[-71°, -58°]$	$[-8°, -6°]$	25°	51°	−7.2236	285.7481	14.8060	0.2784	8.5582	−4.6500
Descending	HH	\	$[-71°, -58°]$	$[-1.5°, 1.5°]$	25°	51°	−4.3802	−1.0861	−0.9552	0.0789	18.4655	−11.4831
Descending	HH	Dry	$[-71°, -58°]$	$[-1.5°, 1.5°]$	25°	51°	−295.8783	−34810.0813	30.6285	296.1303	0.0306	0.1922
Descending	HH	Wet	$[-71°, -58°]$	$[-1.5°, 1.5°]$	25°	51°	572.7618	−577.9363	−0.0034	0.0785	16.6108	−10.2820
Descending	HH	\	$[-71°, -58°]$	$[0°, 2°]$	25°	51°	−4.8100	−0.7779	−1.0996	0.0770	21.8644	−13.2411
Descending	HH	\	$[-71°, -58°]$	$[-4°, -2°]$	25°	51°	−5.4629	−0.0675	−3.8562	0.0916	−19.8794	12.6504
Descending	HH	\	$[-71°, -58°]$	$[-8°, -6°]$	25°	51°	−6.0733	−0.0215	−4.7519	0.1040	22.6048	−14.2082
Ascending	VV	\	$[-66.5°, -54.5°]$	$[-5.5°, -2.5°]$	25°	51°	−0.0139	−10.4268	0.3373	2.9652	2.0058	−0.0785
Ascending	HV	\	$[-65°, -54.5°]$	$[-5°, -3°]$	25°	51°	1060.0836	−299640.0275	35.5740	1073.5357	0.0313	3.1175
Descending	VV	\	$[-66.5°, -54.5°]$	$[-5.5°, -2.5°]$	25°	51°	−5.9958	−0.0218	−4.6197	0.1343	16.7827	−10.5134
Descending	HV	\	$[-65°, -54.5°]$	$[-5°, -3°]$	25°	51°	31.1713	−45.4836	0.0207	0.8476	5.4475	−2.9382

Note: coordinates of the investigated data sets are reported as well, together with acquisition orbit direction and seasonal information.

where $P = [P_1, P_2, P_3, P_4, P_5, P_6]$ is a vector of fitting coefficients, which is estimated through a least-squares optimization as

$$P = \arg\min_P ||\gamma^0_{\text{mean}} - \hat{\gamma}^0_{\text{mean}}||^2 \tag{4}$$

with $\hat{\gamma}^0_{\text{mean}}$ being the derived backscatter model and γ^0_{mean} the computed sample mean of the data distribution. It is important to mention that the local incidence angle θ_l is given to the model in radians.

The resulting fitting parameters (P_1 to P_6) are provided in Table II and refer to the backscatter distributions shown in Figs. 6, 7, 8, and 10. Besides the fitting coefficients and the considered angular range, Table II reports latitude/longitude locations of the considered TDX data for fitting the models as well as the orbit direction of acquisition and seasonal information. If no seasonal description is provided, the models refer to the yearly data sets, where no filtering was performed depending on the acquisition period. Although the resulting coefficients for dry/wet months appear quite different compared with the results without distinguishing between seasons, the corresponding models do not significantly differ, as already shown in Sections IV and V. Actually, the observed differences in the fitting parameters are simply caused by the least-squares minimization procedure.

A fitting example is presented in Fig. 12 over test site (a) and for HH polarization. The measured $\gamma^0_{\text{mean}}(\text{dB})$ values are reported as green/blue point markers for morning/descending orbit and evening/ascending orbit acquisitions, respectively, and are

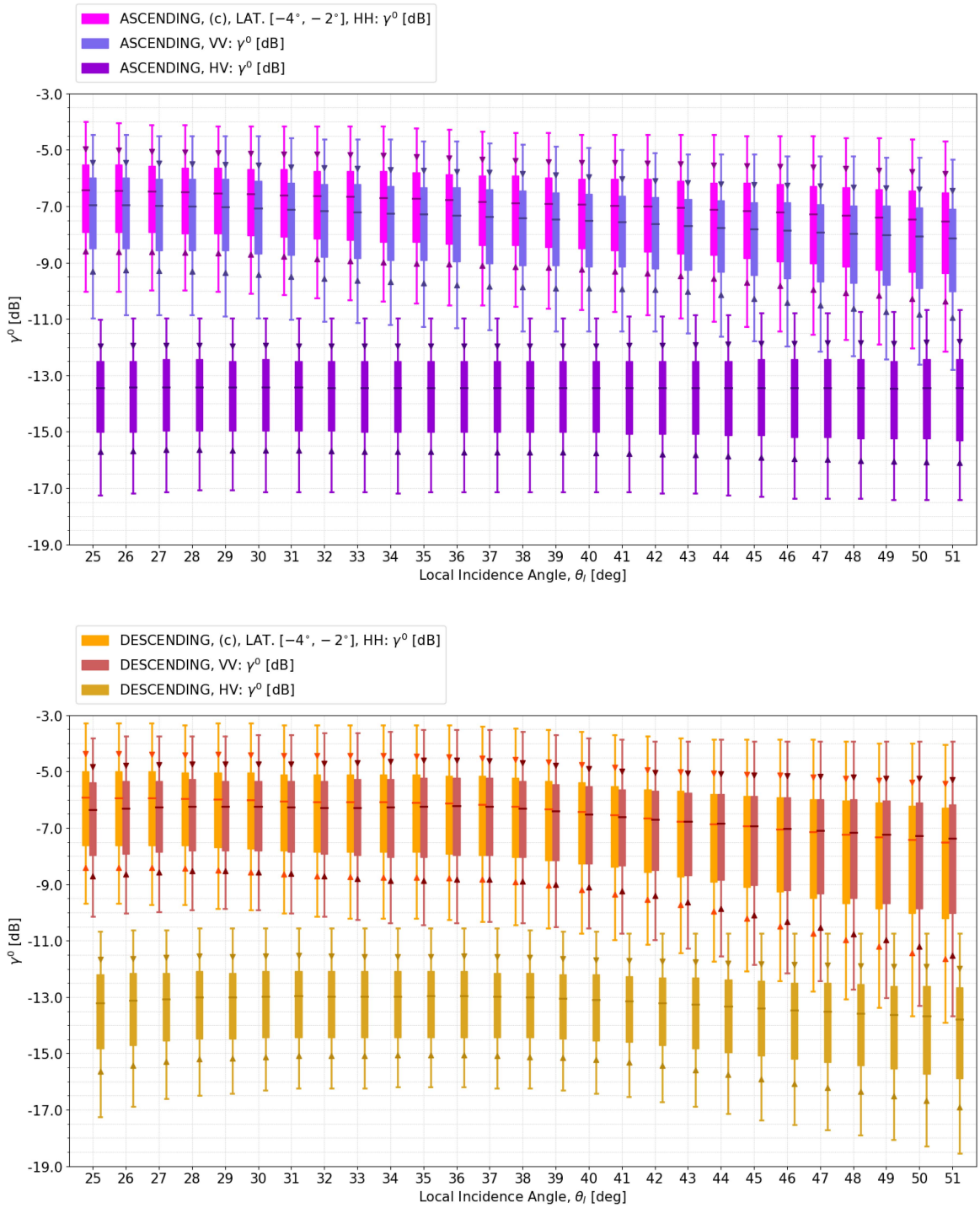

Fig. 10. Comparison of the γ^0 radar backscatter dependency on incidence angle between HH, VV, and HV polarization channels. Data distributions are shown for both data takes acquired in the evening/ascending orbit (top) and in the morning/descending orbit (bottom). Boxes extend from the 25th to 75th percentiles of the data distributions, with whiskers reaching the 5th and 95th percentiles. Solid horizontal lines indicate the mean values of the total distributions, with triangles identifying the corresponding SD confidence intervals, i.e., from mean −SD to mean +SD.

then fitted according to (3) and (4) (green/blue lines). It is worth noting that the assumed nonlinear fitting function precisely estimates the true derived measurements. Moreover, the 50th occurrence intervals of the γ^0 distributions, comprised between 25th and 75th percentiles, are shown as well with respect to local incidence angles. The model provided in [56] and corresponding to forests and orchards (trees) is also depicted (black solid line) for comparison purposes. To this aim, it is important to remind that all the models presented in [56] were derived in dB for the σ^0 backscatter mapping quantity and, therefore, they have to be converted to γ^0 in order to be consistent with the present analysis. The estimated $\hat{\gamma}^0_{\text{mean}}(\text{dB})$ is derived from the $\hat{\sigma}^0_{\text{mean}}(\text{dB})$

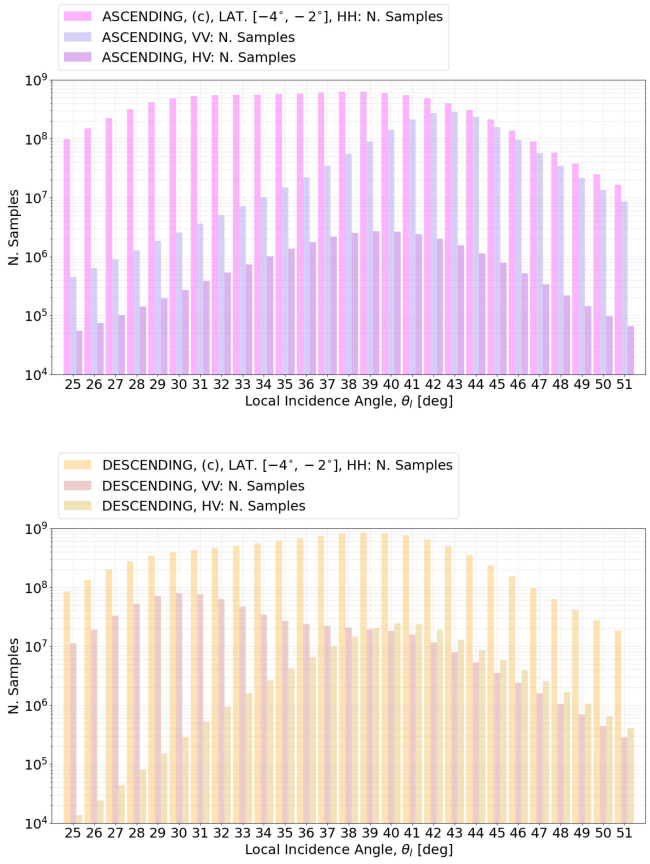

Fig. 11. Histograms in logarithmic scale corresponding to γ^0 distributions in Fig. 10 and depicting the number of samples used for the derivation of the backscatter statistical parameters.

model as

$$\hat{\gamma}^0_{\text{mean}}(\text{dB}) = 10 \cdot \log\left(\frac{10^{\hat{\sigma}^0_{\text{mean}}(\text{dB})/10}}{\cos(\theta_l)}\right). \tag{5}$$

Moreover, the reported 5th (dotted) and 95th (dashed) occurrence levels are derived as in [56], by simply adding $\pm 1.645 \cdot \text{s}(\theta_l)$, where $\text{s}(\theta_l)$ is the SD model. Even though the Ulaby and Dobson models have been used worldwide for a large variety of applications, it can be seen that they do not always precisely represent the radar backscatter when investigating specific test sites, specially when dealing with vegetated areas. This is shown in Fig. 12, where different types of forests are modeled, as suggested by the discrepancy between green/blue and black curves. This is reasonable, as our models refer to the tropical Amazon rainforest, whereas the Ulaby and Dobson one was derived from terrestrial scatterometric measurements over temperate forests in Pennsylvania, USA. Moreover, it is worth noting that the 50th confidence intervals of γ^0 backscatter derived in this work lie within the 90th occurrence range provided by Ulaby and Dobson. As exhaustively discussed in [56], the large variability of the Ulaby and Dobson backscatter model is explained by the wide variations in the magnitude of the radar backscatter among different measurement programs. In particular, this could be explained by a variety of systems and platforms used for in-situ campaigns, as well as by the presence of different on-ground conditions mixed within the same land cover class.

IX. Discussion

Despite appearing to be a quite stable and isotropic target, the Amazon rainforest shows a nonperfectly-isotropic behavior when illuminated using X-band radar waves.

The X-band γ^0 backscatter profile appears to be mostly influenced by the day-time of acquisition, as presented in Section IV. Overall, images acquired in the morning, i.e., with a descending orbit direction, present higher backscatter values, with a bias of about 0.5 dB, when compared with the ones acquired in the evening, i.e., with an ascending orbit geometry. Some considerations could then be formulated, based on the findings in [25] and [75]. First, X-band radar backscatter is probably attenuated during the day-light hours by the high humidity in the air. Then, during night/morning hours, an increase of the radar backscatter could be explained by higher levels of rainwater storage on the tree leaves, due to condensation and cooler air. Moreover, this discrepancy could also be associated to a different amount of rainfall in the afternoon compared with night/morning. In this case, the increase of the radar backscatter caused by rainwater storage on the tree leaves surface could be lower than the backscatter attenuation due to the rainfall itself, resulting in an overall lower scattering. It is worth noting that this overall bias between morning/evening acquisitions is consistent with [11], [12], and [13], where a systematic offset of about 0.3 dB was observed between descending and ascending passes of the RADARSAT-1/2 satellites. In particular, the higher difference observed in X-band compared with C-band is reasonable, as an increased atmospheric attenuation is expected in presence of high humidity, due to the shorter wavelength.

Similar hypotheses could be formulated regarding the γ^0 backscatter dependency on seasonality, presented in Section V. In this case, we did not observe significant differences between dry (June–September) and wet (December–March) seasons. This could be explained by the fact that no predominant scattering effects occur depending on the considered season. Also, it is important to mention that although precipitations reduce during the driest months, the Amazon gets a significant amount of rain throughout the year [74].

Different locations in the Amazon rainforest, characterized by different climate conditions and biomes at large scale [65], [66], [67], [68], [69], [70], are also analyzed in Section VI. The three investigated test sites [see Table I (b)–(d)] show radar backscatter profiles over local incidence angles in agreement with each other, when considering acquisitions performed in the evening, i.e., with an ascending orbit direction. This could be explained by high and uniform levels of humidity during day-light hours, which could result in a more uniform γ^0 backscatter distribution over incidence angles. Moreover, as explained in [25], more attenuation is expected in presence of humid air and for larger incidence angles, as the radar wave propagation path is longer. As a consequence, backscatter profiles tend to converge as moving toward far-range geometries. A different behavior is observed when considering acquisitions performed in the morning, i.e., with a descending orbit configuration. The analysis revealed a more stable backscatter profile over local incidence angles when considering the equatorial rainforest, with a log-backscatter bias around 0.78 dB [test site (a)] and 0.65 dB [test site (b)] between near and far range. When considering the southern test areas, i.e., (c) and (d), the γ^0 backscatter appears less stable along the entire range of illuminated incidence angles,

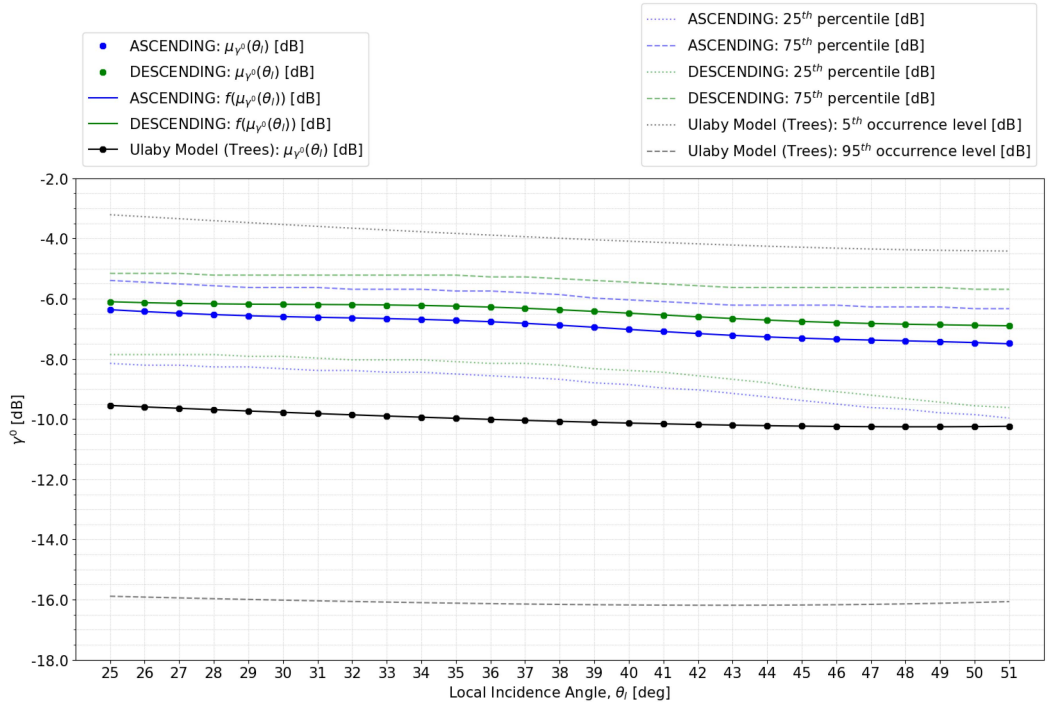

Fig. 12. Nonlinear curve fitting of the γ^0 radar backscatter over test site (a) in Table I and for HH polarization. It refers to morning/descending orbit (green) and evening/ascending orbit (blue) acquisitions. Model-based backscatter estimations are shown with solid lines. Dotted and dashed lines represent confidence levels. $\hat{\gamma}^0$ Ulaby and Dobson model [56], corresponding to forests and orchards (trees), is reported in black together with the corresponding occurrence levels.

with log-backscatter variations higher than 1 dB. This could be explained by different local conditions over these regions, related to, e.g., forest properties themselves (e.g., canopy density and structure) [65], [69], [70] and/or deforestation effects [66], [67], [68], [72], [73]. The presence of rainwater on the tree leaves surface, due to condensation and cooler morning air, could then contribute in different manners to the backscatter: In presence of a lower canopy density, for example, the radar backscatter over larger/shallower incidence angles could be less affected by rainwater, due to a less direct interaction with the canopy leaves, and could be further attenuated by the longer wave propagation path through the vegetation itself [25]. Moreover, changing climate conditions could also contribute to some extent to these instabilities: A different amount of precipitations on a more irregular basis and/or different local humidity levels and temperatures in the air during night/morning hours might then play a nonnegligible role. As a further consideration, it is worth noting that different types of vegetation might also contribute to the different backscatter behaviors and could be mixed in the analysis, due to the large-scale nature of the investigation. Anyhow, the future challenge will be to find reliable reference measurements in order to investigate all these aspects and to better characterize the impact of different climate conditions and biomes on SAR data.

A statistical characterization of the radar backscatter is then presented for VV and HV polarizations in Section VII, using the small amount of available TDX data. An accurate calibration of the copolarized channels, i.e., HH and VV, was ensured over reference calibration point targets, such as corner reflectors and transponders, leading to an overall almost-equal performance [4]. The analysis confirmed the backscatter investigations done during the TDX bistatic commissioning phase, regarding HH and VV polarizations [33]. Indeed, slightly lower backscatter levels are observed from images acquired in vertical copolarization (VV) compared with the horizontal copolarization (HH) channel. This bias appears small and almost negligible for acquisitions performed in the morning; a possible reason for the observed instabilities over the entire range of illuminated incidence angles could be found in the general comments on test site (c) discussed above. On the other hand, a higher bias of about 0.5 dB is observed from acquisitions performed in the evening: This discrepancy is probably caused by the combination of particular scattering mechanisms within the canopy volume and the extremely humid climate of the Amazon rainforest during day-light hours. According to theoretical considerations about randomly-distributed targets, negligible differences between the two copolarizations should be expected after the polarimetric calibration. Nevertheless, the noncompletely-randomly-distributed nature of the scattering mechanisms within the upper layers of the canopy could impact the backscatter in a different way depending on the considered polarization; reflections from the canopy itself could then be more dominant than the radiation coming from the trunk and branches, or vice versa. From the obtained results, all these effects could then be emphasized by the higher humidity in the air and/or by an increased water content on the tree leaves surface due to a larger amount of precipitations during the day-light time compared with night. As far as the HV cross-polarization is concerned, a backscatter drop up to 7 dB is observed. The reason can be found in the intrinsic properties of HV-polarized images, which record the part of the transmitted horizontal-polarized waves, which are redirected back vertically-polarized to the sensor after the interaction with the target on ground. As well

documented in the literature, the HV contribution is lower than that of HH and VV in most cases [76].

Overall, it is important to mention that a higher backscatter variability (wider backscatter confidence intervals) is detected as moving toward larger incidence angles, i.e., far-range geometries. A possible reason could be found in the scattering mechanisms dependency on the incidence angle [75]: Smaller/steeper angles allow the incident wave to penetrate more in the canopy and more likely to reach the ground, resulting in higher branches and trunks contributions. On the other hand, in presence of larger/shallower incidence angles the incident wave has to travel longer through vegetation before reaching the ground, and is more likely affected by specular reflection mechanisms, thus, resulting in higher backscatter variability.

Finally, based on the findings in [25] and [75], a future investigation of other potential and hidden variables could further improve the accuracy of the statistical models provided in this work, e.g., by including precipitation information data or humidity measurements from ground-based radar data. However, the inclusion of additional variables, describing more specific local geophysical processes, will face the lack of ground-truth data over several regions, thus, limiting large-scale studies in favor of smaller and more stationary test sites.

X. Conclusion

In this article, we presented a detailed statistical characterization of γ^0 radar backscatter at X-band over the Amazon rainforest using almost-full resolution TDX data.

Although the Amazon rainforest appears to be a quite stable and isotropic target, analyses over different test sites demonstrated its nonperfectly-isotropic nature, as backscatter profiles slightly decrease with respect to local incidence angles. Overall, morning acquisitions appear brighter than evening ones, confirming that the X-band γ^0 backscatter of the Amazon rainforest is mostly influenced by the day-time of acquisition.

We also provided a statistical characterization of γ^0 backscatter depending on seasonality, by comparing dry and wet seasons. In this case, we did not observe significant differences between the two seasons. Moreover, we analyzed different regions of interest in the Amazon rainforest, characterized by different climate conditions and biomes at large scale. In particular, the analysis revealed more stable local conditions on average over the equatorial rainforest.

Furthermore, a statistical characterization of the radar backscatter was presented for VV and HV polarizations as well. Here, since all nominal TDX data takes are performed in HH polarization, only small data sets were acquired in VV and HV channels for LTSM purposes over selected test sites. Nevertheless, the analysis revealed slightly lower backscatter levels at VV polarization if compared with HH polarization. On the other hand, HV cross-polarized images showed higher backscatter differences compared with copolarized data, i.e., acquired in HH/VV channels, with backscatter values up to 7 dB lower.

In addition, we derived a series of empirical X-band backscatter models over the Amazon rainforest for all the investigated scenarios, based on the analyzed TDX data. To this aim, we relied on the same formulation introduced by Ulaby and Dobson in [56], showing that such models do not precisely represent the radar backscatter when considering tropical vegetated areas, since they were derived from temperate forests.

Never before has a similar investigation at X-band been performed at large scale and in such a detailed manner. Therefore, we are convinced that the derived insights presented in this work can guide users for a proper exploitation of the Amazon basin at X-band in order to define more suitable regions for SAR calibration purposes and to enhance the estimation accuracy of the antenna pattern shape in elevation. Moreover, the proposed analysis could be considered as reference groundwork for future investigations, aiming not only at including additional local geophysical variables but also at extending the study to the characterization of regional climate conditions and biomes from SAR data. The presented results could also motivate a deeper and more accurate investigation of the temporal stability of the Amazon rainforest radiation over stationary test sites in order to monitor the radiometric degradation of current X-band missions over time. Finally, we believe that the models derived in the present analysis represent an extremely valuable input for radar system design and physical modeling purposes, as scientists can utilize them to obtain a very accurate statistical estimation of the γ^0 backscatter over the Amazon rainforest.

Appendix

A summary of all statistical parameters from the investigations performed in Sections IV, V, VI, and VII is presented in this appendix in Table III . In particular, statistical distribution tables over the Amazon rainforest are reported for HH, VV, and HV polarization acquisitions at X-band. As already mentioned, all statistics are computed in linear scale and are here expressed in dB. The γ^0 backscatter distributions are characterized with respect to each interval of local incidence angles θ_l, ranging from near, i.e., 25°, to far range, i.e., 51°. At each incidence angle, the following information is provided:

1) minimum/maximum values, denoted as γ^0_{min} and γ^0_{max}, respectively;
2) 5th, 25th, 50th (median value), 75th, and 95th percentiles, denoted as γ^0_{x}, x being the corresponding percentile;
3) mean value;
4) SD of the distribution; and
5) SEM.

Moreover, it is important to comment about the different statistical meaning of SD and SEM [77], [78], [79]. SD measures the amount of variability, or dispersion, from the individual data values of a distribution to the mean value. Differently, SEM measures how far the sample mean (average) of the data set is likely to be from the true population mean. Thus, SEM describes how precise the mean of the sample is as an estimate of the true mean of the population. The SEM is computed as

$$\text{SEM} = \frac{\text{SD}}{\sqrt{\text{N}}} \tag{6}$$

with N being the size of the sample data. It is worth noting that SEM decreases as the data set size increases, meaning that the sample mean estimates the true mean of the population with greater precision. Finally, all reported values in the table can be directly downloaded in csv format at the web link in [80].

TABLE III
STATISTICS OF γ^0 BACKSCATTER AT X-BAND OVER THE AMAZON RAINFOREST (VALUES ARE IN DB)

γ^0 statistics. **Lon.** $[-71°, -58°]$, **Lat.** $[-1.5°, 1.5°]$: **HH Pol., Ascending**.

θ_{l}	$\gamma^0_{\max}$	γ^0_5	γ^0_{25}	Median	γ^0_{75}	γ^0_{95}	$\gamma^0_{\min}$	Mean	SD	SEM
25°	−2.053	−10.557	−8.152	−6.745	−5.396	−3.578	−13.372	−6.372	−9.746	−52.885
26°	−2.111	−10.499	−8.211	−6.745	−5.455	−3.636	−13.314	−6.421	−9.824	−53.393
27°	−2.229	−10.557	−8.211	−6.804	−5.513	−3.754	−13.314	−6.483	−9.929	−53.934
28°	−2.287	−10.557	−8.270	−6.862	−5.572	−3.812	−13.255	−6.534	−10.007	−54.418
29°	−2.346	−10.557	−8.270	−6.921	−5.630	−3.871	−13.314	−6.574	−10.061	−54.804
30°	−2.346	−10.616	−8.328	−6.921	−5.630	−3.871	−13.372	−6.598	−10.070	−55.063
31°	−2.405	−10.674	−8.387	−6.979	−5.630	−3.871	−13.490	−6.625	−10.087	−55.277
32°	−2.405	−10.733	−8.387	−6.979	−5.689	−3.930	−13.548	−6.644	−10.081	−55.440
33°	−2.405	−10.792	−8.446	−6.979	−5.689	−3.930	−13.666	−6.662	−10.073	−55.568
34°	−2.405	−10.850	−8.446	−7.038	−5.689	−3.930	−13.783	−6.684	−10.069	−55.662
35°	−2.405	−10.968	−8.504	−7.038	−5.748	−3.930	−13.900	−6.715	−10.070	−55.719
36°	−2.463	−11.026	−8.563	−7.097	−5.748	−3.988	−14.018	−6.767	−10.108	−55.773
37°	−2.463	−11.144	−8.622	−7.155	−5.806	−4.047	−14.135	−6.823	−10.133	−55.804
38°	−2.522	−11.202	−8.680	−7.214	−5.865	−4.106	−14.252	−6.887	−10.185	−55.849
39°	−2.581	−11.261	−8.798	−7.331	−5.982	−4.164	−14.370	−6.954	−10.237	−55.869
40°	−2.639	−11.378	−8.856	−7.390	−6.041	−4.223	−14.545	−7.025	−10.282	−55.841
41°	−2.639	−11.554	−8.974	−7.449	−6.100	−4.223	−14.721	−7.095	−10.299	−55.725
42°	−2.639	−11.672	−9.032	−7.566	−6.158	−4.282	−14.956	−7.163	−10.299	−55.500
43°	−2.639	−11.848	−9.150	−7.625	−6.217	−4.282	−15.191	−7.221	−10.275	−55.158
44°	−2.639	−12.082	−9.267	−7.683	−6.217	−4.282	−15.484	−7.271	−10.233	−54.725
45°	−2.581	−12.317	−9.384	−7.742	−6.217	−4.282	−15.777	−7.308	−10.157	−54.211
46°	−2.522	−12.493	−9.501	−7.801	−6.217	−4.223	−16.012	−7.339	−10.080	−53.679
47°	−2.522	−12.727	−9.619	−7.801	−6.276	−4.223	−16.246	−7.378	−10.031	−53.184
48°	−2.463	−12.903	−9.677	−7.859	−6.276	−4.223	−16.422	−7.407	−9.969	−52.692
49°	−2.463	−13.021	−9.795	−7.918	−6.276	−4.223	−16.598	−7.441	−9.932	−52.233
50°	−2.405	−13.196	−9.853	−7.977	−6.334	−4.164	−16.774	−7.467	−9.878	−51.772
51°	−2.346	−13.314	−9.971	−8.035	−6.334	−4.164	−16.891	−7.489	−9.828	−51.325

γ^0 statistics. **Lon.** $[-71°, -58°]$, **Lat.** $[-1.5°, 1.5°]$: **HH Pol., Descending**.

θ_{l}	$\gamma^0_{\max}$	γ^0_5	γ^0_{25}	Median	γ^0_{75}	γ^0_{95}	$\gamma^0_{\min}$	Mean	SD	SEM
25°	−1.877	−10.088	−7.859	−6.452	−5.161	−3.402	−12.551	−6.121	−9.593	−53.133
26°	−1.935	−10.088	−7.859	−6.452	−5.161	−3.402	−12.610	−6.133	−9.621	−53.656
27°	−1.935	−10.088	−7.859	−6.510	−5.161	−3.402	−12.669	−6.145	−9.635	−54.147
28°	−1.935	−10.147	−7.859	−6.510	−5.220	−3.460	−12.727	−6.158	−9.646	−54.567
29°	−1.935	−10.147	−7.918	−6.510	−5.220	−3.460	−12.786	−6.174	−9.647	−54.856
30°	−1.935	−10.205	−7.918	−6.510	−5.220	−3.460	−12.845	−6.192	−9.634	−55.002
31°	−1.935	−10.323	−7.977	−6.569	−5.220	−3.460	−13.021	−6.205	−9.600	−55.055
32°	−1.877	−10.381	−8.035	−6.569	−5.220	−3.402	−13.138	−6.213	−9.555	−55.054
33°	−1.877	−10.440	−8.035	−6.569	−5.220	−3.402	−13.255	−6.220	−9.531	−55.072
34°	−1.877	−10.499	−8.035	−6.569	−5.220	−3.402	−13.372	−6.227	−9.516	−55.096
35°	−1.877	−10.557	−8.094	−6.628	−5.220	−3.402	−13.490	−6.245	−9.510	−55.116
36°	−1.877	−10.674	−8.152	−6.628	−5.279	−3.460	−13.666	−6.277	−9.512	−55.132
37°	−1.935	−10.733	−8.152	−6.686	−5.279	−3.460	−13.783	−6.320	−9.548	−55.184
38°	−1.935	−10.792	−8.211	−6.745	−5.337	−3.519	−13.900	−6.364	−9.567	−55.217
39°	−1.994	−10.909	−8.328	−6.804	−5.396	−3.578	−14.076	−6.420	−9.602	−55.233
40°	−1.994	−11.026	−8.387	−6.862	−5.455	−3.578	−14.252	−6.477	−9.612	−55.175
41°	−2.053	−11.202	−8.446	−6.921	−5.513	−3.636	−14.428	−6.545	−9.643	−55.084
42°	−2.053	−11.320	−8.563	−6.979	−5.572	−3.695	−14.663	−6.607	−9.645	−54.894
43°	−2.053	−11.554	−8.680	−7.038	−5.630	−3.695	−14.956	−6.668	−9.625	−54.571
44°	−1.994	−11.789	−8.798	−7.155	−5.630	−3.695	−15.308	−6.718	−9.553	−54.068
45°	−1.935	−12.082	−8.974	−7.214	−5.630	−3.636	−15.718	−6.763	−9.451	−53.433
46°	−1.877	−12.375	−9.091	−7.273	−5.630	−3.578	−16.070	−6.797	−9.342	−52.769
47°	−1.818	−12.610	−9.208	−7.331	−5.630	−3.519	−16.364	−6.823	−9.244	−52.150
48°	−1.760	−12.845	−9.326	−7.390	−5.630	−3.519	−16.598	−6.845	−9.161	−51.600
49°	−1.701	−13.021	−9.443	−7.390	−5.630	−3.460	−16.833	−6.866	−9.088	−51.101
50°	−1.642	−13.196	−9.560	−7.449	−5.689	−3.460	−17.009	−6.886	−9.022	−50.640
51°	−1.584	−13.372	−9.619	−7.507	−5.689	−3.402	−17.126	−6.905	−8.962	−50.203

γ^0 statistics. **Lon.** $[-71°, -58°]$, **Lat.** $[-1.5°, 1.5°]$: **HH Pol., Ascending, Dry Season**.

θ_{l}	$\gamma^0_{\max}$	γ^0_5	γ^0_{25}	Median	γ^0_{75}	γ^0_{95}	$\gamma^0_{\min}$	Mean	SD	SEM
25°	−1.935	−10.557	−8.094	−6.628	−5.279	−3.460	−13.548	−6.264	−9.577	−48.924
26°	−1.994	−10.557	−8.094	−6.628	−5.279	−3.519	−13.548	−6.297	−9.628	−49.365
27°	−2.053	−10.557	−8.152	−6.686	−5.337	−3.578	−13.548	−6.330	−9.681	−49.807
28°	−2.111	−10.557	−8.152	−6.686	−5.337	−3.578	−13.548	−6.362	−9.738	−50.264
29°	−2.170	−10.557	−8.152	−6.745	−5.396	−3.636	−13.548	−6.395	−9.802	−50.755
30°	−2.229	−10.557	−8.152	−6.745	−5.455	−3.695	−13.490	−6.429	−9.875	−51.288
31°	−2.287	−10.557	−8.211	−6.804	−5.513	−3.754	−13.490	−6.470	−9.951	−51.844
32°	−2.346	−10.557	−8.211	−6.804	−5.513	−3.812	−13.490	−6.513	−10.022	−52.374
33°	−2.405	−10.557	−8.270	−6.862	−5.572	−3.871	−13.490	−6.553	−10.079	−52.808
34°	−2.405	−10.616	−8.270	−6.921	−5.630	−3.871	−13.490	−6.587	−10.105	−53.090
35°	−2.463	−10.674	−8.328	−6.979	−5.689	−3.930	−13.548	−6.634	−10.138	−53.234
36°	−2.463	−10.792	−8.446	−7.038	−5.689	−3.988	−13.666	−6.684	−10.143	−53.208
37°	−2.463	−10.909	−8.504	−7.097	−5.748	−3.988	−13.783	−6.743	−10.152	−53.080
38°	−2.522	−11.026	−8.563	−7.155	−5.806	−4.047	−13.959	−6.812	−10.189	−52.933
39°	−2.522	−11.144	−8.680	−7.214	−5.865	−4.106	−14.135	−6.875	−10.209	−52.734
40°	−2.581	−11.261	−8.739	−7.273	−5.924	−4.106	−14.370	−6.939	−10.236	−52.480
41°	−2.581	−11.437	−8.856	−7.331	−5.982	−4.164	−14.545	−6.994	−10.220	−52.102
42°	−2.581	−11.613	−8.974	−7.390	−6.041	−4.164	−14.839	−7.047	−10.182	−51.626
43°	−2.522	−11.789	−9.032	−7.449	−6.041	−4.164	−15.015	−7.087	−10.120	−51.091
44°	−2.522	−11.965	−9.150	−7.507	−6.041	−4.164	−15.249	−7.129	−10.079	−50.576
45°	−2.463	−12.141	−9.267	−7.566	−6.100	−4.106	−15.425	−7.163	−10.023	−50.057
46°	−2.463	−12.317	−9.326	−7.625	−6.100	−4.106	−15.660	−7.201	−9.988	−49.566
47°	−2.405	−12.434	−9.443	−7.683	−6.100	−4.106	−15.777	−7.231	−9.939	−49.066
48°	−2.405	−12.610	−9.501	−7.742	−6.158	−4.106	−15.953	−7.262	−9.905	−48.590
49°	−2.346	−12.727	−9.560	−7.742	−6.158	−4.106	−16.070	−7.284	−9.854	−48.102
50°	−2.346	−12.845	−9.677	−7.801	−6.158	−4.106	−16.188	−7.311	−9.825	−47.643
51°	−2.287	−12.962	−9.736	−7.859	−6.158	−4.047	−16.305	−7.331	−9.778	−47.176

γ^0 statistics. **Lon.** $[-71°, -58°]$, **Lat.** $[-1.5°, 1.5°]$: **HH Pol., Ascending, Wet Season**.

θ_{l}	$\gamma^0_{\max}$	γ^0_5	γ^0_{25}	Median	γ^0_{75}	γ^0_{95}	$\gamma^0_{\min}$	Mean	SD	SEM
25°	−1.935	−10.557	−8.152	−6.686	−5.279	−3.519	−13.490	−6.310	−9.600	−51.308
26°	−1.994	−10.616	−8.152	−6.686	−5.337	−3.578	−13.490	−6.354	−9.657	−51.722
27°	−2.053	−10.616	−8.211	−6.745	−5.396	−3.578	−13.490	−6.403	−9.716	−52.129
28°	−2.111	−10.674	−8.270	−6.804	−5.455	−3.636	−13.490	−6.449	−9.770	−52.503
29°	−2.170	−10.733	−8.328	−6.862	−5.513	−3.695	−13.548	−6.489	−9.815	−52.819
30°	−2.229	−10.792	−8.328	−6.862	−5.513	−3.754	−13.607	−6.526	−9.855	−53.091
31°	−2.229	−10.792	−8.387	−6.921	−5.572	−3.754	−13.666	−6.560	−9.876	−53.326
32°	−2.287	−10.850	−8.446	−6.921	−5.572	−3.812	−13.783	−6.602	−9.918	−53.564
33°	−2.287	−10.909	−8.446	−6.979	−5.630	−3.812	−13.842	−6.638	−9.940	−53.755
34°	−2.346	−10.968	−8.504	−7.038	−5.689	−3.871	−13.959	−6.683	−9.977	−53.917
35°	−2.346	−11.085	−8.563	−7.097	−5.689	−3.930	−14.076	−6.725	−9.992	−54.016
36°	−2.405	−11.144	−8.622	−7.155	−5.806	−3.988	−14.194	−6.788	−10.048	−54.126
37°	−2.463	−11.202	−8.680	−7.214	−5.865	−4.047	−14.311	−6.855	−10.109	−54.254
38°	−2.522	−11.320	−8.739	−7.273	−5.924	−4.106	−14.428	−6.918	−10.173	−54.380
39°	−2.581	−11.378	−8.798	−7.331	−5.982	−4.164	−14.545	−6.981	−10.228	−54.466
40°	−2.639	−11.437	−8.915	−7.390	−6.041	−4.223	−14.663	−7.044	−10.273	−54.478
41°	−2.639	−11.613	−8.974	−7.449	−6.100	−4.223	−14.839	−7.107	−10.284	−54.378
42°	−2.639	−11.730	−9.091	−7.566	−6.158	−4.282	−15.073	−7.170	−10.277	−54.157
43°	−2.639	−11.965	−9.208	−7.625	−6.158	−4.282	−15.367	−7.226	−10.246	−53.815
44°	−2.581	−12.141	−9.326	−7.683	−6.217	−4.282	−15.660	−7.270	−10.180	−53.374
45°	−2.581	−12.375	−9.443	−7.742	−6.217	−4.282	−15.894	−7.315	−10.130	−52.916
46°	−2.522	−12.551	−9.501	−7.801	−6.276	−4.223	−16.129	−7.350	−10.060	−52.427
47°	−2.522	−12.786	−9.619	−7.859	−6.276	−4.223	−16.364	−7.392	−10.017	−51.963
48°	−2.463	−12.962	−9.736	−7.918	−6.276	−4.223	−16.540	−7.424	−9.960	−51.492
49°	−2.405	−13.079	−9.853	−7.977	−6.276	−4.164	−16.716	−7.453	−9.904	−51.028
50°	−2.405	−13.255	−9.912	−7.977	−6.334	−4.164	−16.891	−7.487	−9.872	−50.593
51°	−2.346	−13.372	−10.029	−8.035	−6.334	−4.164	−17.009	−7.511	−9.822	−50.150

γ^0 statistics. **Lon.** $[-71°, -58°]$, **Lat.** $[-1.5°, 1.5°]$: **HH Pol., Descending, Dry Season**.

θ_{l}	$\gamma^0_{\max}$	γ^0_5	γ^0_{25}	Median	γ^0_{75}	γ^0_{95}	$\gamma^0_{\min}$	Mean	SD	SEM
25°	−1.877	−9.912	−7.742	−6.393	−5.103	−3.343	−12.258	−6.052	−9.593	−50.715
26°	−1.877	−9.912	−7.742	−6.393	−5.103	−3.343	−12.258	−6.044	−9.597	−51.246
27°	−1.877	−9.912	−7.742	−6.393	−5.103	−3.343	−12.317	−6.046	−9.611	−51.795
28°	−1.935	−9.912	−7.742	−6.393	−5.103	−3.402	−12.317	−6.066	−9.654	−52.330
29°	−1.935	−9.971	−7.801	−6.452	−5.161	−3.402	−12.375	−6.099	−9.673	−52.731
30°	−1.994	−10.088	−7.859	−6.510	−5.220	−3.460	−12.551	−6.154	−9.702	−52.991
31°	−1.994	−10.147	−7.918	−6.569	−5.220	−3.519	−12.727	−6.206	−9.702	−53.082
32°	−1.994	−10.264	−7.977	−6.569	−5.279	−3.519	−12.903	−6.244	−9.688	−53.063
33°	−1.994	−10.381	−8.035	−6.628	−5.279	−3.519	−13.138	−6.268	−9.660	−52.951
34°	−1.935	−10.499	−8.094	−6.628	−5.279	−3.460	−13.372	−6.282	−9.605	−52.734
35°	−1.935	−10.616	−8.152	−6.686	−5.279	−3.460	−13.607	−6.310	−9.573	−52.480
36°	−1.935	−10.792	−8.211	−6.686	−5.337	−3.460	−13.783	−6.344	−9.546	−52.209
37°	−1.935	−10.909	−8.270	−6.745	−5.337	−3.460	−13.959	−6.376	−9.523	−51.961
38°	−1.877	−11.026	−8.328	−6.804	−5.337	−3.460	−14.135	−6.399	−9.480	−51.724
39°	−1.877	−11.144	−8.387	−6.804	−5.396	−3.460	−14.370	−6.429	−9.455	−51.514
40°	−1.877	−11.261	−8.504	−6.862	−5.396	−3.460	−14.545	−6.460	−9.427	−51.284
41°	−1.877	−11.437	−8.563	−6.921	−5.396	−3.460	−14.780	−6.496	−9.395	−51.024
42°	−1.818	−11.554	−8.622	−6.921	−5.455	−3.460	−15.015	−6.528	−9.345	−50.726
43°	−1.818	−11.789	−8.739	−6.979	−5.455	−3.460	−15.308	−6.571	−9.315	−50.413
44°	−1.760	−11.965	−8.856	−7.038	−5.513	−3.460	−15.543	−6.609	−9.258	−50.025
45°	−1.760	−12.199	−8.974	−7.097	−5.513	−3.460	−15.836	−6.653	−9.211	−49.607
46°	−1.701	−12.375	−9.091	−7.155	−5.513	−3.402	−16.129	−6.690	−9.143	−49.164
47°	−1.701	−12.610	−9.208	−7.214	−5.572	−3.402	−16.364	−6.728	−9.101	−48.757
48°	−1.642	−12.786	−9.267	−7.273	−5.572	−3.402	−16.540	−6.756	−9.043	−48.358
49°	−1.584	−12.962	−9.384	−7.331	−5.572	−3.343	−16.716	−6.782	−8.988	−47.978
50°	−1.584	−13.138	−9.501	−7.390	−5.572	−3.343	−16.891	−6.814	−8.957	−47.630
51°	−1.525	−13.255	−9.560	−7.449	−5.630	−3.343	−17.009	−6.840	−8.909	−47.273

γ^0 statistics. **Lon.** $[-71°, -58°]$, **Lat.** $[-1.5°, 1.5°]$: **HH Pol., Descending, Wet Season**.

θ_{l}	$\gamma^0_{\max}$	γ^0_5	γ^0_{25}	Median	γ^0_{75}	γ^0_{95}	$\gamma^0_{\min}$	Mean	SD	SEM
25°	−1.818	−10.205	−7.918	−6.452	−5.161	−3.343	−12.786	−6.120	−9.498	−51.031
26°	−1.818	−10.264	−7.918	−6.510	−5.161	−3.343	−12.903	−6.137	−9.491	−51.390
27°	−1.818	−10.323	−7.977	−6.510	−5.161	−3.343	−13.021	−6.158	−9.488	−51.718
28°	−1.818	−10.381	−7.977	−6.569	−5.161	−3.343	−13.079	−6.176	−9.485	−51.992
29°	−1.818	−10.381	−8.035	−6.569	−5.220	−3.343	−13.138	−6.191	−9.478	−52.190
30°	−1.818	−10.499	−8.035	−6.569	−5.220	−3.343	−13.255	−6.205	−9.463	−52.315
31°	−1.760	−10.557	−8.094	−6.569	−5.161	−3.343	−13.372	−6.195	−9.399	−52.395
32°	−1.818	−10.616	−8.152	−6.628	−5.220	−3.343	−13.548	−6.238	−9.425	−52.465
33°	−1.818	−10.674	−8.152	−6.628	−5.220	−3.343	−13.666	−6.260	−9.417	−52.527
34°	−1.818	−10.792	−8.211	−6.686	−5.279	−3.402	−13.783	−6.284	−9.418	−52.602
35°	−1.818	−10.792	−8.211	−6.686	−5.279	−3.402	−13.842	−6.308	−9.427	−52.704
36°	−1.877	−10.850	−8.270	−6.745	−5.337	−3.460	−13.959	−6.342	−9.463	−52.856
37°	−1.877	−10.909	−8.270	−6.745	−5.337	−3.460	−14.018	−6.372	−9.490	−53.034
38°	−1.935	−10.968	−8.328	−6.804	−5.396	−3.519	−14.135	−6.414	−9.542	−53.246
39°	−1.994	−11.026	−8.387	−6.804	−5.455	−3.578	−14.194	−6.461	−9.591	−53.413
40°	−1.994	−11.144	−8.446	−6.862	−5.455	−3.578	−14.370	−6.512	−9.605	−53.458
41°	−2.053	−11.261	−8.563	−6.979	−5.513	−3.636	−14.604	−6.578	−9.626	−53.398
42°	−2.053	−11.496	−8.622	−7.038	−5.572	−3.695	−14.897	−6.644	−9.612	−53.180
43°	−1.994	−11.730	−8.798	−7.097	−5.630	−3.636	−15.191	−6.702	−9.557	−52.792
44°	−1.994	−11.965	−8.915	−7.214	−5.630	−3.636	−15.601	−6.761	−9.500	−52.290
45°	−1.935	−12.258	−9.032	−7.273	−5.689	−3.636	−15.953	−6.804	−9.410	−51.690
46°	−1.877	−12.551	−9.208	−7.331	−5.689	−3.578	−16.305	−6.839	−9.316	−51.074
47°	−1.818	−12.786	−9.326	−7.390	−5.689	−3.519	−16.598	−6.865	−9.228	−50.489
48°	−1.760	−12.962	−9.443	−7.449	−5.689	−3.519	−16.833	−6.887	−9.150	−49.955
49°	−1.701	−13.196	−9.501	−7.449	−5.689	−3.460	−17.009	−6.906	−9.078	−49.464
50°	−1.642	−13.314	−9.619	−7.507	−5.689	−3.460	−17.185	−6.926	−9.013	−49.005
51°	−1.584	−13.490	−9.736	−7.566	−5.689	−3.402	−17.361	−6.946	−8.951	−48.568

TABLE III
(CONTINUED.)

γ^0 statistics. **Lon.** $[-71°, -58°]$, **Lat.** $[0°, 2°]$: **HH Pol., Ascending**.

θ_l	γ^0_{max}	γ^0_5	γ^0_{25}	Median	γ^0_{75}	γ^0_{95}	γ^0_{min}	Mean	SD	SEM
25°	−1.994	−10.440	−8.094	−6.686	−5.337	−3.578	−13.255	−6.339	−9.726	−52.541
26°	−2.111	−10.440	−8.152	−6.745	−5.455	−3.636	−13.255	−6.400	−9.828	−53.089
27°	−2.170	−10.440	−8.211	−6.804	−5.513	−3.754	−13.196	−6.460	−9.918	−53.634
28°	−2.287	−10.499	−8.211	−6.862	−5.572	−3.812	−13.196	−6.522	−10.020	−54.157
29°	−2.346	−10.499	−8.270	−6.921	−5.630	−3.871	−13.196	−6.563	−10.078	−54.557
30°	−2.346	−10.557	−8.328	−6.921	−5.630	−3.871	−13.255	−6.589	−10.087	−54.820
31°	−2.405	−10.616	−8.328	−6.979	−5.630	−3.871	−13.372	−6.616	−10.104	−55.032
32°	−2.405	−10.674	−8.387	−6.979	−5.689	−3.930	−13.490	−6.636	−10.096	−55.189
33°	−2.405	−10.733	−8.387	−6.979	−5.689	−3.930	−13.607	−6.654	−10.086	−55.306
34°	−2.405	−10.850	−8.446	−7.038	−5.689	−3.930	−13.724	−6.676	−10.081	−55.382
35°	−2.405	−10.909	−8.504	−7.038	−5.748	−3.930	−13.842	−6.707	−10.082	−55.420
36°	−2.463	−10.968	−8.563	−7.097	−5.748	−3.988	−13.959	−6.757	−10.114	−55.455
37°	−2.463	−11.085	−8.622	−7.155	−5.806	−4.047	−14.076	−6.813	−10.138	−55.465
38°	−2.522	−11.144	−8.680	−7.214	−5.865	−4.106	−14.194	−6.878	−10.190	−55.494
39°	−2.581	−11.261	−8.739	−7.273	−5.924	−4.164	−14.311	−6.946	−10.245	−55.506
40°	−2.581	−11.320	−8.856	−7.390	−6.041	−4.164	−14.428	−7.011	−10.273	−55.457
41°	−2.639	−11.496	−8.915	−7.449	−6.100	−4.223	−14.604	−7.086	−10.313	−55.358
42°	−2.639	−11.613	−9.032	−7.507	−6.158	−4.282	−14.839	−7.153	−10.314	−55.139
43°	−2.639	−11.789	−9.150	−7.566	−6.158	−4.282	−15.073	−7.211	−10.293	−54.806
44°	−2.639	−12.023	−9.267	−7.683	−6.217	−4.282	−15.367	−7.261	−10.251	−54.376
45°	−2.581	−12.258	−9.326	−7.683	−6.217	−4.282	−15.660	−7.298	−10.174	−53.855
46°	−2.581	−12.434	−9.443	−7.742	−6.217	−4.223	−15.953	−7.336	−10.112	−53.328
47°	−2.522	−12.669	−9.560	−7.801	−6.276	−4.223	−16.188	−7.367	−10.040	−52.800
48°	−2.463	−12.845	−9.677	−7.859	−6.276	−4.223	−16.422	−7.397	−9.975	−52.294
49°	−2.405	−12.962	−9.736	−7.918	−6.276	−4.164	−16.540	−7.421	−9.916	−51.806
50°	−2.405	−13.138	−9.853	−7.977	−6.276	−4.164	−16.716	−7.452	−9.880	−51.354
51°	−2.346	−13.255	−9.912	−7.977	−6.276	−4.164	−16.833	−7.471	−9.827	−50.901

γ^0 statistics. **Lon.** $[-71°, -58°]$, **Lat.** $[-4°, -2°]$: **HH Pol., Ascending**.

θ_l	γ^0_{max}	γ^0_5	γ^0_{25}	Median	γ^0_{75}	γ^0_{95}	γ^0_{min}	Mean	SD	SEM
25°	−2.757	−10.029	−7.918	−6.628	−5.513	−3.988	−12.845	−6.421	−10.455	−50.436
26°	−2.815	−10.029	−7.918	−6.686	−5.513	−4.047	−12.669	−6.454	−10.525	−51.412
27°	−2.815	-9.971	−7.918	−6.686	−5.572	−4.106	−12.610	−6.480	−10.569	−52.328
28°	−2.815	-9.971	−7.977	−6.745	−5.630	−4.106	−12.551	−6.504	−10.601	−53.105
29°	−2.874	−10.029	−7.977	−6.745	−5.630	−4.164	−12.493	−6.532	−10.637	−53.698
30°	−2.874	−10.088	−8.035	−6.804	−5.689	−4.164	−12.551	−6.562	−10.634	−54.060
31°	−2.874	−10.147	−8.094	−6.862	−5.689	−4.164	−12.610	−6.600	−10.625	−54.242
32°	−2.815	−10.264	−8.152	−6.862	−5.748	−4.164	−12.786	−6.634	−10.582	−54.274
33°	−2.815	−10.323	−8.211	−6.921	−5.748	−4.164	−12.903	−6.665	−10.562	−54.273
34°	−2.815	−10.381	−8.270	−6.979	−5.748	−4.164	−12.962	−6.692	−10.557	−54.293
35°	−2.874	−10.440	−8.270	−6.979	−5.806	−4.223	−13.021	−6.732	−10.597	−54.384
36°	−2.933	−10.499	−8.328	−7.038	−5.865	−4.282	−13.021	−6.779	−10.658	−54.511
37°	−2.991	−10.499	−8.387	−7.097	−5.924	−4.340	−13.021	−6.828	−10.726	−54.648
38°	−3.050	−10.557	−8.387	−7.097	−5.924	−4.399	−13.079	−6.874	−10.785	−54.759
39°	−3.050	−10.616	−8.446	−7.155	−5.982	−4.399	−13.079	−6.906	−10.805	−54.775
40°	−3.109	−10.674	−8.504	−7.214	−6.041	−4.457	−13.196	−6.942	−10.822	−54.704
41°	−3.050	−10.733	−8.563	−7.214	−6.041	−4.457	−13.314	−6.968	−10.782	−54.490
42°	−3.050	−10.850	−8.622	−7.273	−6.041	−4.457	−13.490	−7.005	−10.762	−54.193
43°	−3.050	−10.968	−8.680	−7.331	−6.100	−4.457	−13.607	−7.051	−10.752	−53.772
44°	−3.050	−11.085	−8.739	−7.390	−6.158	−4.457	−13.842	−7.107	−10.740	−53.161
45°	−3.050	−11.261	−8.856	−7.449	−6.158	−4.516	−14.076	−7.162	−10.714	−52.344
46°	−2.991	−11.437	−8.974	−7.507	−6.217	−4.516	−14.370	−7.212	−10.661	−51.374
47°	−2.991	−11.613	−9.032	−7.566	−6.276	−4.516	−14.663	−7.270	−10.639	−50.394
48°	−2.991	−11.730	−9.150	−7.625	−6.334	−4.575	−14.897	−7.331	−10.635	−49.447
49°	−3.050	−11.906	−9.267	−7.742	−6.393	−4.575	−15.132	−7.403	−10.668	−48.559
50°	−3.050	−12.023	−9.326	−7.801	−6.452	−4.633	−15.308	−7.468	−10.686	−47.675
51°	−3.109	−12.141	−9.384	−7.859	−6.510	−4.692	−15.425	−7.538	−10.737	−46.823

γ^0 statistics. **Lon.** $[-71°, -58°]$, **Lat.** $[-8°, -6°]$: **HH Pol., Ascending**.

θ_l	γ^0_{max}	γ^0_5	γ^0_{25}	Median	γ^0_{75}	γ^0_{95}	γ^0_{min}	Mean	SD	SEM
25°	−2.815	−10.440	−8.152	−6.862	−5.689	−4.106	−13.314	−6.618	−10.498	−51.506
26°	−2.874	−10.440	−8.211	−6.921	−5.748	−4.164	−13.255	−6.668	−10.573	−52.280
27°	−2.933	−10.440	−8.211	−6.979	−5.806	−4.223	−13.196	−6.718	−10.650	−53.049
28°	−2.991	−10.440	−8.270	−6.979	−5.865	−4.282	−13.138	−6.763	−10.712	−53.740
29°	−2.991	−10.499	−8.328	−7.038	−5.865	−4.340	−13.138	−6.799	−10.733	−54.286
30°	−3.050	−10.557	−8.387	−7.097	−5.924	−4.340	−13.196	−6.839	−10.758	−54.709
31°	−3.050	−10.616	−8.387	−7.097	−5.924	−4.399	−13.255	−6.871	−10.752	−54.969
32°	−2.991	−10.674	−8.446	−7.155	−5.924	−4.340	−13.314	−6.890	−10.715	−55.073
33°	−2.991	−10.733	−8.504	−7.155	−5.982	−4.340	−13.372	−6.908	−10.693	−55.085
34°	−2.991	−10.792	−8.504	−7.214	−5.982	−4.340	−13.431	−6.922	−10.676	−55.045
35°	−2.991	−10.792	−8.563	−7.214	−5.982	−4.340	−13.490	−6.939	−10.673	−55.008
36°	−3.050	−10.850	−8.563	−7.214	−5.982	−4.399	−13.490	−6.967	−10.711	−55.008
37°	−3.050	−10.850	−8.622	−7.273	−6.041	−4.457	−13.490	−6.999	−10.739	−54.989
38°	−3.109	−10.909	−8.680	−7.331	−6.100	−4.457	−13.548	−7.047	−10.793	−54.979
39°	−3.167	−10.968	−8.680	−7.390	−6.158	−4.516	−13.548	−7.100	−10.856	−54.967
40°	−3.226	−11.026	−8.739	−7.449	−6.217	−4.575	−13.607	−7.159	−10.925	−54.947
41°	−3.284	−11.026	−8.798	−7.507	−6.276	−4.692	−13.607	−7.216	−10.990	−54.872
42°	−3.284	−11.085	−8.856	−7.507	−6.334	−4.692	−13.666	−7.261	−11.014	−54.654
43°	−3.343	−11.202	−8.915	−7.566	−6.334	−4.751	−13.724	−7.301	−11.034	−54.285
44°	−3.284	−11.261	−8.974	−7.625	−6.393	−4.692	−13.900	−7.325	−10.982	−53.690
45°	−3.284	−11.437	−9.032	−7.625	−6.393	−4.692	−14.076	−7.350	−10.931	−52.954
46°	−3.226	−11.554	−9.091	−7.683	−6.393	−4.692	−14.252	−7.372	−10.854	−52.108
47°	−3.167	−11.730	−9.208	−7.683	−6.393	−4.633	−14.428	−7.397	−10.779	−51.241
48°	−3.167	−11.848	−9.267	−7.742	−6.393	−4.633	−14.604	−7.431	−10.736	−50.423
49°	−3.109	−11.965	−9.326	−7.801	−6.393	−4.633	−14.721	−7.460	−10.683	−49.625
50°	−3.109	−12.082	−9.443	−7.859	−6.452	−4.633	−14.839	−7.493	−10.658	−48.881
51°	−3.109	−12.199	−9.501	−7.859	−6.452	−4.633	−14.897	−7.520	−10.632	−48.151

γ^0 statistics. **Lon.** $[-71°, -58°]$, **Lat.** $[0°, 2°]$: **HH Pol., Descending**.

θ_l	γ^0_{max}	γ^0_5	γ^0_{25}	Median	γ^0_{75}	γ^0_{95}	γ^0_{min}	Mean	SD	SEM
25°	−1.994	−10.088	−7.801	−6.452	−5.161	−3.460	−12.669	−6.143	−9.726	−51.836
26°	−2.053	−10.088	−7.859	−6.452	−5.220	−3.519	−12.727	−6.162	−9.762	−52.339
27°	−2.053	−10.088	−7.859	−6.510	−5.220	−3.519	−12.786	−6.179	−9.784	−52.824
28°	−2.111	−10.088	−7.859	−6.510	−5.279	−3.578	−12.845	−6.201	−9.821	−53.272
29°	−2.111	−10.147	−7.859	−6.510	−5.279	−3.578	−12.903	−6.213	−9.824	−53.610
30°	−2.111	−10.147	−7.859	−6.510	−5.279	−3.578	−12.962	−6.221	−9.811	−53.845
31°	−2.053	−10.205	−7.918	−6.510	−5.279	−3.519	−12.962	−6.215	−9.768	−53.983
32°	−2.053	−10.264	−7.918	−6.510	−5.220	−3.519	−13.021	−6.212	−9.746	−54.110
33°	−2.053	−10.264	−7.918	−6.510	−5.220	−3.519	−13.079	−6.212	−9.730	−54.221
34°	−2.053	−10.323	−7.918	−6.510	−5.220	−3.519	−13.196	−6.223	−9.720	−54.305
35°	−2.053	−10.381	−7.977	−6.569	−5.279	−3.519	−13.314	−6.248	−9.721	−54.360
36°	−2.053	−10.440	−8.035	−6.628	−5.337	−3.578	−13.431	−6.289	−9.734	−54.391
37°	−2.111	−10.557	−8.094	−6.686	−5.396	−3.636	−13.548	−6.346	−9.780	−54.430
38°	−2.111	−10.616	−8.152	−6.745	−5.455	−3.636	−13.666	−6.402	−9.810	−54.435
39°	−2.170	−10.674	−8.211	−6.804	−5.513	−3.695	−13.842	−6.464	−9.856	−54.431
40°	−2.170	−10.792	−8.270	−6.862	−5.572	−3.754	−13.959	−6.522	−9.877	−54.364
41°	−2.170	−10.909	−8.328	−6.921	−5.572	−3.754	−14.135	−6.579	−9.886	−54.229
42°	−2.170	−11.026	−8.446	−6.979	−5.630	−3.812	−14.370	−6.627	−9.871	−53.985
43°	−2.170	−11.202	−8.504	−7.038	−5.630	−3.812	−14.604	−6.663	−9.825	−53.603
44°	−2.111	−11.437	−8.622	−7.038	−5.630	−3.754	−14.897	−6.686	−9.727	−53.071
45°	−2.053	−11.672	−8.739	−7.097	−5.630	−3.695	−15.191	−6.704	−9.606	−52.452
46°	−1.935	−11.965	−8.856	−7.155	−5.630	−3.636	−15.484	−6.713	−9.463	−51.803
47°	−1.877	−12.199	−8.974	−7.155	−5.630	−3.578	−15.777	−6.729	−9.352	−51.213
48°	−1.818	−12.375	−9.091	−7.214	−5.572	−3.519	−16.012	−6.746	−9.257	−50.675
49°	−1.701	−12.551	−9.208	−7.273	−5.572	−3.460	−16.188	−6.755	−9.153	−50.166
50°	−1.701	−12.727	−9.267	−7.273	−5.572	−3.460	−16.364	−6.778	−9.097	−49.733
51°	−1.642	−12.903	−9.384	−7.331	−5.572	−3.402	−16.481	−6.793	−9.031	−49.317

γ^0 statistics. **Lon.** $[-71°, -58°]$, **Lat.** $[-4°, -2°]$: **HH Pol., Descending**.

θ_l	γ^0_{max}	γ^0_5	γ^0_{25}	Median	γ^0_{75}	γ^0_{95}	γ^0_{min}	Mean	SD	SEM
25°	−1.818	−9.677	−7.625	−6.276	−4.985	−3.284	−12.082	−5.927	−9.543	−49.194
26°	−1.818	−9.677	−7.625	−6.276	−4.985	−3.284	−12.023	−5.934	−9.561	−50.200
27°	−1.818	−9.736	−7.625	−6.276	−4.985	−3.284	−12.023	−5.949	−9.577	−51.095
28°	−1.877	−9.736	−7.625	−6.276	−5.044	−3.343	−12.082	−5.970	−9.596	−51.800
29°	−1.818	−9.853	−7.683	−6.334	−5.044	−3.284	−12.199	−5.984	−9.557	−52.230
30°	−1.818	−9.912	−7.742	−6.334	−5.044	−3.284	−12.375	−6.014	−9.535	−52.502
31°	−1.818	−10.029	−7.801	−6.393	−5.103	−3.343	−12.551	−6.048	−9.517	−52.684
32°	−1.818	−10.147	−7.859	−6.393	−5.103	−3.343	−12.786	−6.071	−9.497	−52.840
33°	−1.818	−10.205	−7.859	−6.452	−5.103	−3.343	−12.903	−6.081	−9.481	−53.009
34°	−1.818	−10.205	−7.859	−6.452	−5.103	−3.343	−12.962	−6.086	−9.476	−53.211
35°	−1.818	−10.205	−7.859	−6.452	−5.103	−3.343	−13.021	−6.099	−9.484	−53.436
36°	−1.818	−10.264	−7.918	−6.452	−5.161	−3.343	−13.021	−6.119	−9.499	−53.671
37°	−1.877	−10.323	−7.977	−6.510	−5.161	−3.402	−13.079	−6.162	−9.540	−53.920
38°	−1.935	−10.440	−8.035	−6.569	−5.220	−3.460	−13.196	−6.229	−9.588	−54.143
39°	−1.994	−10.557	−8.152	−6.686	−5.337	−3.519	−13.372	−6.320	−9.642	−54.286
40°	−2.053	−10.733	−8.270	−6.804	−5.396	−3.578	−13.666	−6.428	−9.697	−54.296
41°	−2.111	−10.968	−8.387	−6.921	−5.513	−3.695	−13.959	−6.542	−9.752	−54.160
42°	−2.170	−11.144	−8.563	−7.038	−5.630	−3.754	−14.252	−6.653	−9.793	−53.843
43°	−2.229	−11.437	−8.739	−7.155	−5.689	−3.812	−14.663	−6.759	−9.807	−53.298
44°	−2.229	−11.730	−8.915	−7.273	−5.806	−3.871	−15.073	−6.854	−9.772	−52.513
45°	−2.170	−12.082	−9.091	−7.390	−5.865	−3.871	−15.601	−6.943	−9.701	−51.554
46°	−2.170	−12.434	−9.267	−7.507	−5.924	−3.871	−16.070	−7.036	−9.654	−50.557
47°	−2.170	−12.786	−9.501	−7.625	−5.982	−3.871	−16.540	−7.131	−9.621	−49.569
48°	−2.170	−13.079	−9.677	−7.742	−6.041	−3.930	−16.891	−7.227	−9.607	−48.619
49°	−2.170	−13.372	−9.853	−7.859	−6.100	−3.988	−17.243	−7.324	−9.604	−47.703
50°	−2.229	−13.666	−10.029	−7.977	−6.217	−3.988	−17.537	−7.424	−9.626	−46.834
51°	−2.229	−13.900	−10.205	−8.094	−6.276	−4.047	−17.771	−7.516	−9.635	−45.973

γ^0 statistics. **Lon.** $[-71°, -58°]$, **Lat.** $[-8°, -6°]$: **HH Pol., Descending**.

θ_l	γ^0_{max}	γ^0_5	γ^0_{25}	Median	γ^0_{75}	γ^0_{95}	γ^0_{min}	Mean	SD	SEM
25°	−2.053	−10.147	−8.035	−6.628	−5.337	−3.578	−12.551	−6.284	−9.777	−50.695
26°	−2.111	−10.205	−8.035	−6.686	−5.396	−3.578	−12.610	−6.328	−9.819	−51.468
27°	−2.111	−10.264	−8.094	−6.745	−5.396	−3.636	−12.669	−6.367	−9.837	−52.151
28°	−2.111	−10.323	−8.152	−6.745	−5.455	−3.636	−12.727	−6.395	−9.839	−52.703
29°	−2.111	−10.381	−8.152	−6.745	−5.455	−3.636	−12.845	−6.409	−9.823	−53.109
30°	−2.111	−10.440	−8.211	−6.804	−5.455	−3.636	−13.021	−6.413	−9.795	−53.397
31°	−2.111	−10.499	−8.211	−6.745	−5.396	−3.636	−13.079	−6.405	−9.767	−53.593
32°	−2.053	−10.557	−8.211	−6.745	−5.396	−3.578	−13.196	−6.386	−9.716	−53.696
33°	−2.053	−10.557	−8.211	−6.745	−5.337	−3.578	−13.255	−6.368	−9.692	−53.771
34°	−2.053	−10.557	−8.152	−6.686	−5.337	−3.578	−13.314	−6.356	−9.678	−53.835
35°	−2.053	−10.616	−8.211	−6.686	−5.337	−3.578	−13.372	−6.361	−9.680	−53.932
36°	−2.053	−10.616	−8.211	−6.745	−5.396	−3.578	−13.372	−6.386	−9.694	−54.065
37°	−2.111	−10.674	−8.270	−6.804	−5.455	−3.636	−13.490	−6.439	−9.736	−54.248
38°	−2.111	−10.792	−8.328	−6.862	−5.513	−3.695	−13.607	−6.503	−9.766	−54.423
39°	−2.170	−10.909	−8.446	−6.979	−5.572	−3.754	−13.724	−6.584	−9.821	−54.576
40°	−2.229	−11.085	−8.563	−7.038	−5.689	−3.812	−13.959	−6.676	−9.871	−54.623
41°	−2.287	−11.202	−8.680	−7.155	−5.748	−3.871	−14.194	−6.770	−9.913	−54.538
42°	−2.346	−11.437	−8.798	−7.273	−5.806	−3.930	−14.487	−6.857	−9.938	−54.292
43°	−2.346	−11.613	−8.915	−7.331	−5.865	−3.930	−14.780	−6.930	−9.921	−53.842
44°	−2.346	−11.906	−9.091	−7.390	−5.924	−3.988	−15.132	−6.996	−9.880	−53.206
45°	−2.287	−12.141	−9.208	−7.507	−5.924	−3.930	−15.543	−7.053	−9.804	−52.422
46°	−2.229	−12.434	−9.384	−7.566	−5.982	−3.930	−15.953	−7.108	−9.731	−51.585
47°	−2.229	−12.669	−9.501	−7.683	−6.041	−3.930	−16.305	−7.172	−9.693	−50.767
48°	−2.229	−12.903	−9.619	−7.742	−6.100	−3.930	−16.598	−7.238	−9.666	−49.967
49°	−2.229	−13.138	−9.795	−7.859	−6.100	−3.988	−16.833	−7.304	−9.646	−49.179
50°	−2.229	−13.372	−9.912	−7.918	−6.158	−3.988	−17.067	−7.373	−9.632	−48.405
51°	−2.170	−13.548	−10.088	−8.035	−6.217	−3.988	−17.302	−7.436	−9.599	−47.617

TABLE III
(CONTINUED.)

γ^0 statistics. **Lon.** $[-66.5°, -54.5°]$, **Lat.** $[-5.5°, -2.5°]$: **VV Polarization, Ascending**.

θ_l	$\gamma^0_{\max}$	γ^0_5	γ^0_{25}	Median	γ^0_{75}	γ^0_{95}	$\gamma^0_{\min}$	Mean	SD	SEM
25°	−3.109	−10.968	−8.504	−7.155	−5.982	−4.457	−14.018	−6.959	−10.757	−39.024
26°	−3.167	−10.850	−8.504	−7.155	−5.982	−4.457	−13.842	−6.956	−10.802	−39.806
27°	−3.167	−10.850	−8.563	−7.214	−6.041	−4.516	−13.783	−6.984	−10.827	−40.605
28°	−3.226	−10.850	−8.563	−7.214	−6.041	−4.516	−13.783	−7.002	−10.853	−41.389
29°	−3.226	−10.909	−8.563	−7.273	−6.041	−4.516	−13.783	−7.023	−10.853	−42.153
30°	−3.226	−10.968	−8.680	−7.331	−6.100	−4.516	−13.900	−7.076	−10.859	−42.915
31°	−3.284	−11.026	−8.739	−7.390	−6.158	−4.575	−13.900	−7.127	−10.902	−43.704
32°	−3.284	−11.085	−8.798	−7.449	−6.217	−4.633	−13.959	−7.171	−10.907	−44.422
33°	−3.284	−11.144	−8.856	−7.449	−6.217	−4.633	−14.018	−7.210	−10.912	−45.173
34°	−3.343	−11.202	−8.915	−7.507	−6.276	−4.633	−14.076	−7.249	−10.935	−45.969
35°	−3.343	−11.261	−8.915	−7.566	−6.334	−4.692	−14.135	−7.287	−10.949	−46.799
36°	−3.343	−11.320	−8.974	−7.625	−6.334	−4.692	−14.194	−7.330	−10.970	−47.714
37°	−3.402	−11.378	−9.032	−7.625	−6.393	−4.751	−14.252	−7.372	−11.012	−48.708
38°	−3.402	−11.437	−9.091	−7.683	−6.452	−4.809	−14.252	−7.408	−11.044	−49.749
39°	−3.460	−11.437	−9.091	−7.742	−6.510	−4.868	−14.194	−7.454	−11.116	−50.868
40°	−3.578	−11.437	−9.150	−7.801	−6.569	−4.927	−14.135	−7.507	−11.221	−51.981
41°	−3.636	−11.437	−9.150	−7.801	−6.628	−4.985	−14.076	−7.559	−11.317	−52.935
42°	−3.695	−11.437	−9.208	−7.859	−6.686	−5.103	−14.018	−7.618	−11.413	−53.595
43°	−3.754	−11.496	−9.267	−7.977	−6.745	−5.161	−14.076	−7.686	−11.484	−53.781
44°	−3.812	−11.613	−9.326	−8.035	−6.804	−5.161	−14.252	−7.754	−11.504	−53.368
45°	−3.754	−11.789	−9.443	−8.094	−6.862	−5.161	−14.545	−7.810	−11.441	−52.432
46°	−3.754	−11.965	−9.560	−8.152	−6.862	−5.220	−14.897	−7.863	−11.394	−51.297
47°	−3.754	−12.141	−9.677	−8.211	−6.921	−5.220	−15.191	−7.914	−11.370	−50.154
48°	−3.754	−12.317	−9.736	−8.270	−6.979	−5.220	−15.484	−7.962	−11.356	−49.049
49°	−3.754	−12.434	−9.795	−8.328	−6.979	−5.279	−15.777	−8.017	−11.347	−47.994
50°	−3.754	−12.610	−9.912	−8.387	−7.038	−5.279	−16.070	−8.073	−11.342	−46.995
51°	−3.812	−12.786	−10.029	−8.446	−7.097	−5.337	−16.305	−8.141	−11.364	−46.045

γ^0 statistics. **Lon.** $[-66.5°, -54.5°]$, **Lat.** $[-5.5°, -2.5°]$: **VV Polarization, Descending**.

θ_l	$\gamma^0_{\max}$	γ^0_5	γ^0_{25}	Median	γ^0_{75}	γ^0_{95}	$\gamma^0_{\min}$	Mean	SD	SEM
25°	−2.463	−10.147	−7.977	−6.628	−5.396	−3.812	−12.610	−6.353	−10.125	−45.362
26°	−2.405	−10.029	−7.918	−6.569	−5.337	−3.754	−12.493	−6.306	−10.103	−46.519
27°	−2.405	-9.971	−7.859	−6.510	−5.337	−3.754	−12.317	−6.264	−10.115	−47.716
28°	−2.405	-9.912	−7.801	−6.510	−5.279	−3.754	−12.258	−6.237	−10.120	−48.719
29°	−2.405	-9.853	−7.801	−6.510	−5.337	−3.754	−12.199	−6.238	−10.120	−49.357
30°	−2.346	-9.912	−7.801	−6.510	−5.337	−3.695	−12.317	−6.250	−10.079	−49.583
31°	−2.346	−10.029	−7.859	−6.569	−5.337	−3.695	−12.434	−6.264	−10.040	−49.453
32°	−2.287	−10.147	−7.918	−6.569	−5.337	−3.636	−12.610	−6.275	−9.956	−48.958
33°	−2.170	−10.264	−7.977	−6.569	−5.279	−3.636	−12.903	−6.282	−9.831	−48.188
34°	−2.111	−10.381	−8.035	−6.569	−5.279	−3.578	−13.079	−6.272	−9.729	−47.388
35°	−2.053	−10.440	−8.035	−6.569	−5.220	−3.519	−13.196	−6.235	−9.660	−46.799
36°	−2.053	−10.381	−7.977	−6.510	−5.220	−3.519	−13.196	−6.212	−9.671	−46.555
37°	−2.053	−10.323	−7.977	−6.569	−5.220	−3.519	−13.138	−6.230	−9.706	−46.445
38°	−2.111	−10.381	−8.035	−6.628	−5.337	−3.578	−13.196	−6.305	−9.769	−46.350
39°	−2.170	−10.499	−8.152	−6.745	−5.455	−3.695	−13.255	−6.408	−9.866	−46.309
40°	−2.287	−10.557	−8.270	−6.862	−5.513	−3.812	−13.314	−6.513	−9.985	−46.285
41°	−2.346	−10.733	−8.328	−6.921	−5.630	−3.871	−13.490	−6.606	−10.040	−46.004
42°	−2.346	−10.968	−8.504	−7.038	−5.689	−3.930	−13.842	−6.692	−10.018	−45.350
43°	−2.287	−11.261	−8.680	−7.155	−5.748	−3.930	−14.252	−6.773	−9.940	−44.432
44°	−2.229	−11.554	−8.856	−7.214	−5.806	−3.871	−14.721	−6.849	−9.856	−43.464
45°	−2.229	−11.848	−9.032	−7.331	−5.865	−3.930	−15.191	−6.941	−9.812	−42.543
46°	−2.170	−12.141	−9.208	−7.449	−5.924	−3.930	−15.601	−7.016	−9.746	−41.627
47°	−2.170	−12.434	−9.326	−7.566	−5.982	−3.930	−16.070	−7.087	−9.693	−40.686
48°	−2.111	−12.727	−9.501	−7.625	−5.982	−3.930	−16.422	−7.153	−9.637	−39.742
49°	−2.111	−13.021	−9.677	−7.742	−6.041	−3.930	−16.774	−7.222	−9.594	−38.781
50°	−2.111	−13.314	−9.853	−7.801	−6.100	−3.930	−16.950	−7.285	−9.538	−37.768
51°	−2.053	−13.666	−10.029	−7.977	−6.158	−3.930	−17.302	−7.378	−9.482	−36.776

γ^0 statistics. **Lon.** $[-65°, -54.5°]$, **Lat.** $[-5°, -3°]$: **HV Polarization, Ascending**.

θ_l	$\gamma^0_{\max}$	γ^0_5	γ^0_{25}	Median	γ^0_{75}	γ^0_{95}	$\gamma^0_{\min}$	Mean	SD	SEM
25°	−9.736	−17.243	−15.015	−13.666	−12.493	−11.026	−19.531	−13.452	−17.366	−41.069
26°	−9.795	−17.185	−15.015	−13.666	−12.493	−10.968	−19.531	−13.426	−17.345	−41.686
27°	−9.795	−17.126	−14.956	−13.607	−12.434	−10.968	−19.413	−13.416	−17.382	−42.416
28°	−9.736	−17.067	−14.956	−13.607	−12.434	−10.968	−19.296	−13.410	−17.372	−43.128
29°	−9.795	−17.067	−14.956	−13.666	−12.493	−10.968	−19.238	−13.424	−17.395	−43.853
30°	−9.795	−17.126	−14.956	−13.666	−12.434	−10.968	−19.296	−13.420	−17.373	−44.539
31°	−9.795	−17.126	−14.956	−13.666	−12.493	−10.968	−19.296	−13.427	−17.389	−45.310
32°	−9.736	−17.126	−14.956	−13.666	−12.493	−10.968	−19.296	−13.432	−17.376	−46.021
33°	−9.736	−17.126	−15.015	−13.666	−12.493	−10.968	−19.238	−13.438	−17.359	−46.709
34°	−9.736	−17.185	−15.015	−13.666	−12.493	−10.968	−19.238	−13.441	−17.350	−47.372
35°	−9.736	−17.126	−15.015	−13.666	−12.493	−10.968	−19.179	−13.444	−17.354	−48.010
36°	−9.677	−17.126	−15.015	−13.666	−12.493	−10.968	−19.179	−13.445	−17.336	−48.553
37°	−9.677	−17.126	−15.015	−13.724	−12.493	−10.968	−19.120	−13.445	−17.345	−49.017
38°	−9.677	−17.126	−15.015	−13.724	−12.493	−10.968	−19.120	−13.447	−17.346	−49.341
39°	−9.677	−17.126	−15.015	−13.724	−12.493	−10.968	−19.120	−13.453	−17.341	−49.494
40°	−9.677	−17.126	−15.015	−13.724	−12.493	−10.968	−19.120	−13.452	−17.318	−49.437
41°	−9.619	−17.126	−15.073	−13.724	−12.493	−10.909	−19.120	−13.448	−17.278	−49.177
42°	−9.619	−17.185	−15.073	−13.724	−12.493	−10.909	−19.179	−13.445	−17.245	−48.760
43°	−9.560	−17.185	−15.073	−13.724	−12.493	−10.850	−19.179	−13.444	−17.184	−48.157
44°	−9.501	−17.243	−15.132	−13.724	−12.493	−10.850	−19.179	−13.446	−17.131	−47.415
45°	−9.443	−17.302	−15.132	−13.724	−12.434	−10.792	−19.179	−13.440	−17.063	−46.551
46°	−9.443	−17.361	−15.191	−13.783	−12.434	−10.792	−19.238	−13.447	−17.036	−45.624
47°	−9.443	−17.361	−15.191	−13.783	−12.434	−10.792	−19.296	−13.445	−16.993	−44.647
48°	−9.384	−17.361	−15.249	−13.783	−12.434	−10.733	−19.296	−13.453	−16.947	−43.658
49°	−9.384	−17.419	−15.249	−13.842	−12.493	−10.733	−19.296	−13.473	−16.961	−42.766
50°	−9.326	−17.419	−15.249	−13.783	−12.434	−10.674	−19.296	−13.453	−16.891	−41.826
51°	−9.208	−17.419	−15.308	−13.783	−12.434	−10.674	−19.296	−13.433	−16.831	−40.950

γ^0 statistics. **Lon.** $[-65°, -54.5°]$, **Lat.** $[-5°, -3°]$: **HV Polarization, Descending**.

θ_l	$\gamma^0_{\max}$	γ^0_5	γ^0_{25}	Median	γ^0_{75}	γ^0_{95}	$\gamma^0_{\min}$	Mean	SD	SEM
25°	−9.326	−17.243	−14.839	−13.431	−12.199	−10.674	−23.402	−13.205	−16.880	−37.542
26°	−9.384	−16.891	−14.721	−13.372	−12.141	−10.616	−21.935	−13.130	−16.985	−38.922
27°	−9.267	−16.598	−14.545	−13.314	−12.141	−10.616	−20.117	−13.066	−17.025	−40.221
28°	−9.267	−16.481	−14.487	−13.255	−12.082	−10.557	−19.648	−13.008	−17.028	−41.571
29°	−9.267	−16.422	−14.487	−13.255	−12.141	−10.557	−19.238	−13.001	−17.057	−42.967
30°	−9.208	−16.305	−14.428	−13.255	−12.082	−10.557	−18.827	−12.973	−17.061	−44.369
31°	−9.208	−16.246	−14.428	−13.196	−12.082	−10.557	−18.534	−12.948	−17.067	−45.694
32°	−9.267	−16.246	−14.428	−13.255	−12.082	−10.557	−18.299	−12.969	−17.126	−47.006
33°	−9.267	−16.246	−14.428	−13.255	−12.082	−10.557	−18.299	−12.973	−17.134	−48.175
34°	−9.267	−16.188	−14.428	−13.255	−12.082	−10.557	−18.182	−12.969	−17.139	−49.257
35°	−9.267	−16.188	−14.428	−13.255	−12.082	−10.557	−18.182	−12.969	−17.138	−50.246
36°	−9.267	−16.188	−14.428	−13.255	−12.082	−10.557	−18.123	−12.969	−17.137	−51.195
37°	−9.267	−16.246	−14.428	−13.255	−12.141	−10.557	−18.182	−12.983	−17.139	−52.118
38°	−9.267	−16.246	−14.428	−13.255	−12.141	−10.616	−18.182	−13.010	−17.164	−52.997
39°	−9.326	−16.305	−14.487	−13.314	−12.199	−10.674	−18.240	−13.047	−17.202	−53.753
40°	−9.384	−16.422	−14.545	−13.372	−12.199	−10.674	−18.358	−13.098	−17.229	−54.183
41°	−9.384	−16.540	−14.604	−13.431	−12.258	−10.733	−18.475	−13.150	−17.219	−54.110
42°	−9.384	−16.716	−14.721	−13.490	−12.317	−10.733	−18.768	−13.207	−17.174	−53.538
43°	−9.326	−16.891	−14.839	−13.548	−12.317	−10.733	−19.120	−13.267	−17.092	−52.648
44°	−9.326	−17.126	−14.956	−13.607	−12.375	−10.733	−19.413	−13.333	−17.040	−51.715
45°	−9.326	−17.361	−15.073	−13.724	−12.434	−10.733	−19.765	−13.401	−16.987	−50.778
46°	−9.267	−17.537	−15.191	−13.783	−12.493	−10.733	−20.000	−13.461	−16.923	−49.859
47°	−9.267	−17.713	−15.308	−13.842	−12.493	−10.733	−20.293	−13.519	−16.875	−48.910
48°	−9.208	−17.889	−15.425	−13.959	−12.551	−10.733	−20.469	−13.576	−16.822	−47.928
49°	−9.208	−18.065	−15.543	−14.018	−12.610	−10.733	−20.645	−13.628	−16.770	−46.904
50°	−9.150	−18.299	−15.718	−14.076	−12.610	−10.733	−20.821	−13.680	−16.704	−45.783
51°	−9.150	−18.534	−15.894	−14.194	−12.669	−10.733	−20.997	−13.778	−16.680	−44.699

REFERENCES

[1] M. Schwerdt, D. Hounam, J.–L. Alvarez–Pères, and T. Molkenthin, "The calibration concept of TerraSAR–X: A multiple–mode, high–resolution SAR," *Can. J. Remote Sens.*, vol. 31, no. 1, pp. 30–36, 2005.

[2] M. Schwerdt, B. Brautigam, M. Bachmann, B. Döring, D. Schrank, and J. H. Gonzalez, "Final TerraSAR–X calibration results based on novel efficient methods," *IEEE Trans. Geosci. Remote Sens.*, vol. 48, no. 2, pp. 677–689, Feb. 2010.

[3] B. Brautigam, J. H. Gonzalez, M. Schwerdt, and M. Bachmann, "TerraSAR–X instrument calibration results and extension for TanDEM–X," *IEEE Trans. Geosci. Remote Sens.*, vol. 48, no. 2, pp. 702–715, Feb. 2010.

[4] M. Schwerdt, D. Schrank, M. Bachmann, C. Schulz, B. Döring, and J. H. Gonzales, "TerraSAR–X re–calibration and dual receive antenna campaigns performed in 2009," in *Proc. 8th Eur. Conf. Synthetic Aperture Radar VDE*, 2010, pp. 1–4.

[5] M. Schwerdt et al., "In–orbit calibration of the TanDEM–X system," in *Proc. IEEE Int. Geosci. Remote Sens. Symp.*, 2011, pp. 2420–2423.

[6] M. Schwerdt et al., "Calibration of the TerraSAR–X and the TanDEM–X satellite for the TerraSAR–X mission," in *Proc. 9th Eur. Conf. Synthetic Aperture Radar VDE*, 2012, pp. 56–59.

[7] M. Schwerdt et al., "Independent verification of the Sentinel–1 A system calibration," *IEEE J. Sel. Topics Appl. Earth Observ. Remote Sens.*, vol. 9, no. 3, pp. 994–1007, Mar. 2016.

[8] M. Schwerdt et al., "Independent system calibration of Sentinel–1B," *Remote Sens.*, vol. 9, no. 6, p. 511, 2017.

[9] M. Shimada and A. Freeman, "A technique for measurement of spaceborne SAR antenna patterns using distributed targets," *IEEE Trans. Geosci. Remote Sens.*, vol. 33, no. 1, pp. 100–114, Jan. 1995.

[10] R. Hawkins et al., "Stability of Amazon backscatter at C–band: Spaceborne results from ERS–1/2 and RADARSAT–1," in *Proc. SAR Workshop: CEOS Committee Earth Observ. Satell.*, 2000, p. 99.

[11] A. P. Luscombe and A. Thompson, "RADARSAT–2 calibration: Proposed targets and techniques," in *Proc. IEEE Scanning Present Resolving Future Int. Geosci. Remote Sens. Symp.*, 2001, pp. 496–498.

[12] A. P. Luscombe, "Radiometric calibration information from RADARSAT–1 amazon measurements," in *Proc. CEOS SAR Workshop*, 2001, pp. 2–5.

[13] A. Luscombe, "RADARSAT–2 SAR image quality and calibration operations," *Can. J. Remote Sens.*, vol. 30, no. 3, pp. 345–354, 2004.

[14] J. A.–Perez, M. Schwerdt, and M. Bachmann, "TerraSAR–X antenna pattern estimation by a complex treatment of rain forest measurements," in *Proc. IEEE Int. Symp. Geosci. Remote Sens.*, 2006, pp. 3857–3860.

[15] M. Bachmann, M. Schwerdt, and B. Brautigam, "TerraSAR–X antenna calibration and monitoring based on a precise antenna model," *IEEE Trans. Geosci. Remote Sens.*, vol. 48, no. 2, pp. 690–701, Feb. 2010.

[16] J. W. Antony et al., "Radiometric accuracy and stability of TerraSAR–X and TanDEM–X," in *Proc. EUSAR 11th Eur. Conf. Synthetic Aperture Radar VDE*, 2016, pp. 1–4.

[17] M. Schwerdt et al., "Radiometric performance of the TerraSAR–X mission over more than ten years of operation," *Remote Sens.*, vol. 10, no. 5, p. 754, 2018.

[18] A. Bojarski et al., "TanDEM–X long–term system performance after 10 years of operation," *IEEE J. Sel. Topics Appl. Earth Observ. Remote Sens.*, vol. 14, pp. 2522–2534, 2021.

[19] P. Klenk, K. Schmidt, T. Kraus, M. Bachmann, and M. Schwerdt, "TerraSAR–X/TanDEM–X mission and calibration status," in *Proc. EUSAR 14th Eur. Conf. Synthetic Aperture Radar VDE*, 2022, pp. 1–5.

[20] R. Touzi, M. Shimada, T. Motohka, and S. Nedelcu, "Assessment of PALSAR–2 compact non–circularity using amazonian rainforests," *IEEE Trans. Geosci. Remote Sens.*, vol. 58, no. 10, pp. 7472–7482, Oct. 2020.

[21] Z. Bartalis, W. Wagner, V. Naeimi, D. Sabel, and C. Pathe, "SAR calibration requirements for soil moisture estimation," in *Proc. CEOS SAR Calibration Validation Workshop*, 2009.

[22] S. Cote, S. Srivastava, S. Muir, and T. Lukowsk, "Assessment of distributed target sites within the RADARSAT program," in *Proc. CEOS SAR Calibration Validation Workshop*, 2011.

[23] P. Rizzoli, B. Braeutigam, and M. Zink, "TanDEM–X large–scale study of tropical rainforests for spaceborne SAR calibration in X–band," in *Proc. EUSAR 10th Eur. Conf. Synthetic Aperture Radar*, 2014, pp. 1–4.

[24] I. H. Woodhouse, J. J. V. D. Sanden, and D. H. Hoekman, "Scatterometer observations of seasonal backscatter variation over tropical rain forest," *IEEE Trans. Geosci. Remote Sens.*, vol. 37, no. 2, pp. 859–861, Mar. 1999.

[25] A. Danklmayer, B. J. Doring, M. Schwerdt, and M. Chandra, "Assessment of atmospheric propagation effects in SAR images," *IEEE Trans. Geosci. Remote Sens.*, vol. 47, no. 10, pp. 3507–3518, Oct. 2009.

[26] R. Werninghaus and S. Buckreuss, "The TerraSAR–X mission and system design," *IEEE Trans. Geosci. Remote Sens.*, vol. 48, no. 2, pp. 606–614, Feb. 2010.

[27] H. Breit, T. Fritz, U. Balss, M. Lachaise, A. Niedermeier, and M. Vonavka, "TerraSAR–X SAR processing and products," *IEEE Trans. Geosci. Remote Sens.*, vol. 48, no. 2, pp. 727–740, Feb. 2010.

[28] J. Mittermayer, M. Younis, R. Metzig, S. Wollstadt, J. M. Martínez, and A. Meta, "TerraSAR–X system performance characterization and verification," *IEEE Trans. Geosci. Remote Sens.*, vol. 48, no. 2, pp. 660–676, Feb. 2010.

[29] G. Krieger et al., "TanDEM–X: A satellite formation for high–resolution SAR interferometry," *IEEE Trans. Geosci. Remote Sens.*, vol. 45, no. 11, pp. 3317–3341, Nov. 2007.

[30] S. Huber, M. Younis, and G. Krieger, "The TanDEM–X mission: Overview and interferometric performance," *Int. J. Microw. Wirel. Technol.*, vol. 2, no. 3–4, pp. 379–389, Jul. 2010.

[31] G. Krieger et al., "TanDEM–X: A radar interferometer with two formation–flying satellites," *Acta Astronautica*, vol. 89, pp. 83–98, 2013.

[32] M. Zink et al., "TanDEM–X: 10 years of formation flying bistatic SAR interferometry," *IEEE J. Sel. Topics Appl. Earth Observ. Remote Sens.*, vol. 14, pp. 3546–3565, Feb. 2021.

[33] M. Martone, B. Braeutigam, P. Rizzoli, C. Gonzalez, M. Bachmann, and G. Krieger, "Coherence evaluation of TanDEM–X interferometric data," *ISPRS J. Photogrammetry Remote Sens.*, vol. 73, pp. 21–29, Sep. 2012.

[34] P. Rizzoli, M. Martone, and B. Braeutigam, "Global interferometric coherence maps from TanDEM–X quicklook data," *IEEE Geosci. Remote Sens. Lett.*, vol. 11, no. 11, pp. 1861–1865, Nov. 2014.

[35] P. Rizzoli et al., "Generation and performance assessment of the global TanDEM–X digital elevation model," *ISPRS J. Photogrammetry Remote Sens.*, vol. 132, pp. 119–139, Oct. 2017.

[36] DLR, "TanDEM–X ground segment – experimental product description," DLR, Oberpfaffenhofen, Germany, DLR Rep. TD–GS–PS–3028, Jan. 2012.

[37] F. Kugler, D. Schulze, I. Hajnsek, H. Pretzsch, and K. Papathanassiou, "TanDEM–X Pol–InSAR performance for forest height estimation," *IEEE Trans. Geosci. Remote Sens.*, vol. 52, no. 10, pp. 6404–6422, Oct. 2014.

[38] M. J. Soja, H. Persson, and L. Ulander, "Estimation of forest height and canopy density from a single InSAR correlation coefficient," *IEEE Geosci. Remote Sens. Lett.*, vol. 12, no. 3, pp. 646–650, Mar. 2015.

[39] H. Chen, S. Cloude, D. G. Goodenough, D. A. Hill, and A. Nesdoly, "Radar forest height estimation in mountainous terrain using TanDEM–X coherence data," *IEEE J. Sel. Topics Appl. Earth Observ. Remote Sens.*, vol. 11, no. 10, pp. 3443–3452, Oct. 2018.

[40] M. Nannini et al., "Coherence–based SAR tomography for spaceborne applications," *Remote Sens. Environ.*, vol. 225, pp. 107–114, Jun. 2019.

[41] M. Schlund, P. Magdon, B. Eaton, C. Aumann, and S. Erasmi, "Canopy height estimation with TanDEM–X in temperate and boreal forests," *Int. J. Appl. Earth Observ. Geoinf.*, vol. 82, Oct. 2019, Art. no. 101904.

[42] R. Guliaev, V. C.–Bes, M. Pardini, and K. Papathanassiou, "Forest height estimation by means of TanDEM–X InSAR and waveform lidar data," *IEEE J. Sel. Topics Appl. Earth Observ. Remote Sens.*, vol. 14, pp. 3084–3094, 2021.

[43] R. Treuhaft et al., "Tropical–forest biomass estimation at X–band from the spaceborne TanDEM–X interferometer," *IEEE Geosci. Remote Sens. Lett.*, vol. 12, no. 2, pp. 239–243, Feb. 2015.

[44] W. Qi and R. O. Dubayah, "Combining TanDEM–X InSAR and simulated GEDI lidar observations for forest structure mapping," *Remote Sens. Environ.*, vol. 187, pp. 253–266, Dec. 2016.

[45] J. Askne, M. Soja, and L. Ulander, "Biomass estimation in a boreal forest from TanDEM–X data, LiDAR DTM, and the interferometric water cloud model," *Remote Sens. Environ.*, vol. 196, pp. 265–278, Jul. 2017.

[46] H. Persson, M. Soja, J. Fransson, and M. Ulander, "National forest biomass mapping using the two–level model," *IEEE J. Sel. Topics Appl. Earth Observ. Remote Sens.*, vol. 13, pp. 6391–6400, 2020.

[47] E. Erten, C. Rossi, and O. Yüzügüllü, "Polarization impact in TanDEM–X data over vertical–oriented vegetation: The paddy–rice case study," *IEEE Geosci. Remote Sens. Lett.*, vol. 12, no. 7, pp. 1501–1505, Jul. 2015.

[48] J. L.–Sanchez, F. V.–Guijalba, E. Erten, M. C.–Taberner, and F. G.–Haro, "Retrieval of vegetation height in rice fields using polarimetric SAR interferometry with TanDEM–X data," *Remote Sens. Environ.*, vol. 192, pp. 30–44, Apr. 2017.

[49] M. Schlund, F. V. Poncet, D. H. Hoeckman, S. Kuntz, and C. Schmullius, "Importance of bistatic SAR features from TanDEM–X for forest mapping and monitoring," *Remote Sens. Environ.*, vol. 151, pp. 16–26, Aug. 2014.

[50] M. Martone et al., "The global forest/non–forest map from TanDEM–X interferometric SAR data," *Remote Sens. Environ.*, vol. 205, pp. 352–373, Feb. 2018.

[51] A. Mazza, F. Sica, P. Rizzoli, and G. Scarpa, "TanDEM–X forest mapping using convolutional neural networks," *Remote Sens.*, vol. 11, 2019, Art. no. 2980.

[52] P. Rizzoli, M. Martone, H. Rott, and A. Moreira, "Characterization of snow facies on the Greenland ice sheet observed by TanDEM–X interferometric SAR data," *Remote Sens.*, vol. 9, no. 4, p. 315, Mar. 2017.

[53] G. Fischer, K. Papathanassiou, and I. Hajnsek, "Modeling multifrequency Pol–InSAR data from the percolation zone of the Greenland ice sheet," *IEEE Trans. Geosci. Remote Sens.*, vol. 57, no. 4, pp. 1963–1976, Apr. 2019.

[54] S. Abdullahi, B. Wessel, M. Huber, A. Wendleder, A. Roth, and C. Kuenzer, "Estimating penetration–related X–band InSAR elevation bias: A study over the Greenland ice sheet," *Remote Sens.*, vol. 11, 2019, Art. no. 2903.

[55] H. Rott et al., "Penetration of interferometric radar signals in antarctic snow," *Cryosphere*, vol. 15, pp. 4399–4419, Sep. 2021.

[56] F. Ulaby and M. Craig Dobson, *Handbook of Radar Scattering Statistics for Terrain*. Norwood, MA, USA: Artech House Publishers, 1989.

[57] R. K. Raney, A. Freeman, R. W. Hawkins, and R. Bamler, "A plea for radar brightness," in *Proc. Int. Geosci. Remote Sens. Symp.*, 1994, pp. 1090–1092.

[58] H. Zebker, F. Charbonneau, and D. Small, "Sigma/gamma/beta–nought pros and cons: Calibration and use of terrain corrected products in the age of geocoded single look complex radar image," in *Proc. CEOS SAR Cal–Val Workshop*, 2023.

[59] P. Prats et al., "TAXI: A versatile processing chain for experimental TanDEM–X product evaluation," in *Proc. IEEE Geosci. Remote Sens. Symp.*, 2010, pp. 1–4.

[60] T. Fritz, C. Rossi, N. Y.–Martinez, F. R.–Gonzalez, M. Lachaise, and H. Breit, "Interferometric processing of TanDEM–X data," in *Proc. IEEE Int. Geosci. Remote Sens. Symp.*, 2011, pp. 2428–2431.

[61] C. Gonzalez, M. Bachmann, J. B.–Bello, P. Rizzoli, and M. Zink, "A fully automatic algorithm for editing the TanDEM–X global DEM," *Remote Sens.*, vol. 12, no. 23, Dec. 2020, Art. no. 3961.

[62] C. Choi, M. Pardini, J. Armston, K. P. Papathanassiou, and R. Dubayah, "Relating TanDEM–X local InSAR phase center variations to LiDAR full waveforms over forest scenarios," in *Proc. EUSAR 12th Eur. Conf. Synthetic Aperture Radar VDE*, 2018, pp. 1–4.

[63] D. Carcereri, P. Rizzoli, D. Ienco, and L. Bruzzone, "A deep learning framework for the estimation of forest height from bistatic TanDEM–X data," *IEEE J. Sel. Topics Appl. Earth Observ. Remote Sens.*, vol. 16, pp. 8334–8352, 2023.

[64] M. Bachmann et al., "The TanDEM–X mission phases–ten years of bistatic acquisition and formation planning," *IEEE J. Sel. Topics Appl. Earth Observ. Remote Sens.*, vol. 14, pp. 3504–3518, 2021.

[65] E. E. Sano et al., "Comparative analysis of the global forest/non–forest maps derived from SAR and optical sensors. case studies from Brazilian Amazon and cerrado biomes," *Remote Sens.*, vol. 13, no. 3, p. 367, 2021.

[66] J. Barlow et al., "Anthropogenic disturbance in tropical forests can double biodiversity loss from deforestation," *Nature*, vol. 535, no. 7610, pp. 144–147, 2016.

[67] D. Zemp, C.–F. Schleussner, H. D. M. J. Barbosa, and A. Rammig, "Deforestation effects on Amazon forest resilience," *Geophysical Res. Lett.*, vol. 44, no. 12, pp. 6182–6190, 2017.

[68] D. V. Spracklen, S. R. Arnold, and C. Taylor, "Observations of increased tropical rainfall preceded by air passage over forests," *Nature*, vol. 489, no. 7415, pp. 282–285, 2012.

[69] C. N. Koyama, M. Watanabe, M. Hayashi, T. Ogawa, and M. Shimada, "Mapping the spatial–temporal variability of tropical forests by ALOS–2 l–band SAR Big Data analysis," *Remote Sens. Environ.*, vol. 233, 2019, Art. no. 111372.
[70] S. Saatchi, M. Marlier, R. L. Chazdon, D. B. Clark, and A. E. Russell, "Impact of spatial variability of tropical forest structure on radar estimation of aboveground biomass," *Remote Sens. Environ.*, vol. 115, no. 11, pp. 2836–2849, 2011.
[71] N. Butt, P. A. De Oliveira, and M. H. Costa, "Evidence that deforestation affects the onset of the rainy season in Rondonia, Brazil," *J. Geophysical Res.: Atmos.*, vol. 116, no. D11, 2011.
[72] R. R. Da Silva, D. Werth, and R. Avissar, "Regional impacts of future land–cover changes on the amazon basin wet–season climate," *J. Climate*, vol. 21, no. 6, pp. 1153–1170, 2008.
[73] A. J. Negri, R. F. Adler, L. Xu, and J. Surratt, "The impact of Amazonian deforestation on dry season rainfall," *J. Climate*, vol. 17, no. 6, pp. 1306–1319, 2004.
[74] National Aeronautics and Space Administration (NASA), "Satellite senses subtle amazon seasonality," Accessed: Dec. 13, 2023. [Online]. Available: https://earthobservatory.nasa.gov/images/148363/satellite--senses--subtle--amazon--seasonality
[75] J. J. De Jong, W. Klaassen, and P. J. Kuiper, "Monitoring of rain water storage in forests with satellite radar," *IEEE Trans. Geosci. Remote Sens.*, vol. 40, no. 2, pp. 338–347, 2002.
[76] D. Massonnet and J. C. Souyris, *Imaging With Synthetic Aperture Radar*. Lausanne, Switzerland: EPFL Press, 2008.
[77] D. K. Lee, J. In, and S. Lee, "Standard deviation and standard error of the mean," *Korean J. Anesthesiol.*, vol. 68, no. 3, pp. 220–223, 2015.
[78] D. G. Altman and J. M. Bland, "Standard deviations and standard errors," *Bmj*, vol. 331, no. 7521, p. 903, 2005.
[79] M. P. Barde and P. J. Barde, "What to use to express the variability of data: Standard deviation or standard error of mean?," *Perspectives Clin. Res.*, vol. 3, no. 3, p. 113, 2012.
[80] DLR, "DLR radar science group GitHub page," May 2023. [Online]. Available: https://github.com/DLRRadarScienceGroup

Luca Dell'Amore received the M.Sc. degree in information and communication engineering from the Università degli Studi di Trento, Trento, Italy, in 2019.

Since 2021, he has been a Research Engineer with the Satellite SAR Systems Department, Microwaves and Radar Institute, DLR. He is currently working on performance investigation for the TerraSAR–X and TanDEM–X missions. His master thesis titled "Assessment of Image Quality of Waveform–Encoded Synthetic Aperture Radar (SAR) Using Real Data" has been pursued at the Microwaves and Radar Institute, German Aerospace Center (DLR), Wessling, Germany. His research activities include the development of innovative methods for Sentinel–1 data–based applications. His current research interests include the investigation of distributed SAR systems, with a particular focus on multiple–input multiple–output (MIMO) SAR.

Mr. Dell'Amore was the recipient of a German Academic Exchange Service (DAAD) Scholarship for a doctorate degree in the Radar Concepts Department, Microwaves and Radar Institute, DLR, in 2019. He was also the recipient of the Young Scientist Awards at the International Radar Symposium and Kleinheubacher Tagung, both in 2019.

José–Luis Bueso–Bello received the Ingeniero degree in telecommunications engineering from the Universidad Politécnica de Valencia, Valencia, Spain, in 2003, and the M.Sc. degree in Earth–oriented space science and technology from the Technische Universität München, Munich, Germany, in 2007.

In 2003, he started working with the Microwaves and Radar Institute, German Aerospace Center (DLR), Oberpfaffenhofen, Germany, as System Engineer with the Department of Reconnaissance and Security, where he worked in the definition, design, and mission analysis for different SAR projects. In 2010, he joined the Satellite SAR Systems Department, where he is currently a Project Engineer with main focus on the plan, evaluation, and performance monitoring of the TanDEM–X SAR acquisitions and their image quality assessment. His main research interests include signal processing, Earth system monitoring, and artificial intelligence algorithms applied to SAR images.

Patrick Klenk received the doctoral degree in physics from Heidelberg University, Heidelberg, Germany, in 2012. His Ph.D. dissertation was titled "Ground–Penetrating Radar for Quantitative Soil Hydrology."

After three more years of Postdoctoral work with the Heidelberg University's Institute of Environmental Physics, he joined the German Aerospace Center's Microwaves and Radar Institute in 2016. He is a Senior Research Scientist with the SAR Calibration Center of DLR's Microwaves and Radar Institute, Oberpfaffenhofen, Germany. Since 2018, he has been heading SAR system calibration related projects for various ESA missions and mission proposals such as ROSE–L, Sentinel–1NG, LEOB and HydroTerra, and most recently BIOMASS. On behalf of ESA, he is also currently leading a team responsible for planning and implementing DLR's independent SAR calibration campaign during the in–orbit commissioning of the upcoming Sentinel–1 C mission on behalf of ESA. His current research interests include developing novel SAR calibration techniques with the focus on antenna aspects for current and future satellite SAR systems, such as Tandem–L, TerraSAR–X, TanDEM–X, PAZ, and ESA's Sentinel–1 A/B/C/D, while also being partially responsible for instrument operations of the TerraSAR–X and Tandem–X missions.

Jens Reimann received the M.Sc. degree in information and communication technology from the University of Chemnitz, Chemnitz, Germany, and in cooperation with the Institute of Atmospheric Physics of the German Aerospace Center (DLR), in 2009 and the Ph.D. degree in polarimetric calibration of weather radar systems from the University of Chemnitz, in 2013.

In 2013, he joined the calibration group of the Satellite SAR Systems Department with the Microwaves and Radar Institute, DLR. He led the calibration activities for DLR's Tandem–L system and HRWS. Since 2017, he is in–charge of the end–to–end SAR system calibration for ESA's ROSE–L systems. His current research interests include the development of reference targets for SAR system calibration, such as the transponders/PARCs for ESA's Sentinel–1 mission.

Paola Rizzoli received the B.Sc. and M.Sc. degrees in telecommunication engineering from the Politecnico di Milano University (Polimi), Milan, Italy, in 2003 and 2006, respectively, and the Ph.D. degree (summa cum laude) in electrical engineering and information technology from the Karlsruhe Institute of Technology (KIT), Karlsruhe, Germany, in 2018.

From 2006 to 2008, she was a Scientific Researcher and Project Engineer with the Politecnico di Milano and Aresys, s.r.l., Milan, Italy, a Polimi spin–off company. In 2008, she joined the Microwaves and Radar Institute with the German Aerospace Center (DLR), Oberpfaffenhofen, Germany, as Project Engineer, where she has been involved in the development and optimization of the TerraSAR–X and TanDEM–X missions, concentrating, in particular, on the generation of the TanDEM–X global digital elevation model. From 2016 to 2020, she led the System Performance Research Group of the Satellite SAR Systems Department, being responsible for the final performance assessment of the global TanDEM–X DEM and the generation of the global TanDEM–X forest/nonforest map. Since 2020, she has been leading the Radar Science Research Group. Her main research interests include SAR systems design, data reduction techniques, estimation theory, signal processing, and artificial intelligence algorithms.

Dr. Rizzoli was the recipient of the DLR Science Award in 2018 and the Best Paper Award at the German Microwave Conference in 2019. She is a regular Reviewer for IEEE TRANSACTIONS ON GEOSCIENCE AND REMOTE SENSING, IEEE GEOSCIENCE AND REMOTE SENSING LETTERS and IEEE JOURNAL OF SELECTED TOPICS IN APPLIED EARTH OBSERVATIONS AND REMOTE SENSING.